

1           **Structural and functional ramifications of antigenic drift**  
2                                   **in recent SARS-CoV-2 variants**

3 Meng Yuan<sup>1,\*</sup>, Deli Huang<sup>2,\*</sup>, Chang-Chun D. Lee<sup>1,\*</sup>, Nicholas C. Wu<sup>3,4,\*</sup>, Abigail M.  
4 Jackson<sup>1</sup>, Xueyong Zhu<sup>1</sup>, Hejun Liu<sup>1</sup>, Linghang Peng<sup>2</sup>, Marit J. van Gils<sup>5</sup>, Rogier W.  
5 Sanders<sup>5,6</sup>, Dennis R. Burton<sup>2,7</sup>, S. Momsen Reincke<sup>8,9</sup>, Harald Prüss<sup>8,9</sup>, Jakob Kreye<sup>8,9</sup>,  
6 David Nemazee<sup>2</sup>, Andrew B. Ward<sup>1</sup>, Ian A. Wilson<sup>1,10,§</sup>

7  
8 <sup>1</sup> Department of Integrative Structural and Computational Biology, The Scripps Research  
9 Institute, La Jolla, CA 92037, USA

10 <sup>2</sup> Department of Immunology and Microbiology, The Scripps Research Institute, La Jolla,  
11 CA 92037, USA

12 <sup>3</sup> Department of Biochemistry, University of Illinois at Urbana-Champaign, Urbana, IL  
13 61801, USA

14 <sup>4</sup> Carl R. Woese Institute for Genomic Biology, University of Illinois at Urbana-  
15 Champaign, Urbana, IL 61801, USA

16 <sup>5</sup> Department of Medical Microbiology and Infection Prevention, Amsterdam University  
17 Medical Centers, Location AMC, University of Amsterdam, Amsterdam, The Netherlands

18 <sup>6</sup> Department of Microbiology and Immunology, Weill Medical College of Cornell  
19 University, New York, NY 10021, USA

20 <sup>7</sup> Ragon Institute of MGH, Harvard and MIT, Cambridge, MA 02139, USA

21 <sup>8</sup> German Center for Neurodegenerative Diseases (DZNE) Berlin, Berlin, Germany

22 <sup>9</sup> Department of Neurology and Experimental Neurology, Charité-Universitätsmedizin  
23 Berlin, corporate member of Freie Universität Berlin, Humboldt-Universität Berlin, and  
24 Berlin Institute of Health, Berlin, Germany

25 <sup>10</sup> The Skaggs Institute for Chemical Biology, The Scripps Research Institute, La Jolla,  
26 CA, 92037, USA

27 \* These authors contributed equally to this work

28 § Correspondence: [wilson@scripps.edu](mailto:wilson@scripps.edu) (I.A.W.)

29 **Abstract**

30 The protective efficacy of neutralizing antibodies (nAbs) elicited during natural infection  
31 with SARS-CoV-2 and by vaccination based on its spike protein has been compromised  
32 with emergence of the recent SARS-CoV-2 variants. Residues E484 and K417 in the  
33 receptor-binding site (RBS) are both mutated in lineages first described in South Africa  
34 (B.1.351) and Brazil (B.1.1.28.1). The nAbs isolated from SARS-CoV-2 patients are  
35 preferentially encoded by certain heavy-chain germline genes and the two most frequently  
36 elicited antibody families (IGHV3-53/3-66 and IGHV1-2) can each bind the RBS in two  
37 different binding modes. However, their binding and neutralization are abrogated by either  
38 the E484K or K417N mutation, whereas nAbs to the cross-reactive CR3022 and S309  
39 sites are largely unaffected. This structural and functional analysis illustrates why  
40 mutations at E484 and K417 adversely affect major classes of nAbs to SARS-CoV-2 with  
41 consequences for next-generation COVID-19 vaccines.

42

## 43 INTRODUCTION

44 The COVID-19 pandemic has already lasted for over a year, but new infections are still  
45 escalating throughout the world. While several different COVID-19 vaccines have been  
46 deployed globally, a major concern is the emergence of antigenically distinct SARS-CoV-  
47 2 variants. In particular, the B.1.351 (also known as 501Y.V2) lineage in South Africa (1)  
48 and B.1.1.28 lineage (and its descendant B.1.1.28.1, also known as P.1) in Brazil (2) have  
49 raised serious questions about the nature, extent and consequences of the antigenic drift  
50 observed in circulating SARS-CoV-2. The B.1.351 and B.1.1.28.1 lineages both share  
51 three mutations, namely K417N/T, E484K, and N501Y (which is also present in the UK  
52 B.1.1.7 lineage). A few B.1.1.7 genomes with the E484K mutation have also recently been  
53 detected (3). All of these mutations are located in the receptor binding site (RBS) of the  
54 receptor binding domain (RBD) of the spike (S) protein (Figure 1A). Two of these three  
55 mutations, K417N and E484K, decrease the neutralizing activity of sera as well as of  
56 monoclonal antibodies isolated from COVID-19 convalescent plasma and vaccinated  
57 individuals (4-10). Previous studies have shown that certain IGHV genes are highly  
58 enriched in the antibody response to SARS-CoV-2 infection, especially IGHV3-53 (11-15)  
59 and IGHV1-2 (12, 16, 17). IGHV3-53 and IGHV3-66, which differ by only one conservative  
60 substitution V12I, and IGHV1-2 are the most enriched IGHV genes used among 1,593  
61 RBD antibodies from 32 studies (12-43) (Figure 1B). Thus, we have investigated the  
62 effects of these mutations on neutralization of SARS-CoV-2 by multi-donor class  
63 antibodies, and the consequences for current vaccines and therapeutics.

64

65 We tested the activity of a panel of 18 neutralizing antibodies isolated from COVID-19  
66 patients or humanized mice against wild-type (Wuhan) SARS-CoV-2 pseudovirus, as well  
67 as single mutants K417N and E484K (Figure 1C). Neutralization of four and five antibodies  
68 out of the 18 tested antibodies were abolished by K417N and E484K, respectively.



69 Strikingly, neutralization by all six highly potent IGHV3-53/3-66 antibodies that we tested  
70 was diminished for either K417N (binding mode 1) or E484K (binding mode 2) mutations  
71 (Figure 1C-D). In addition, neutralization by IGHV1-2 antibodies was strongly reduced in  
72 the E484K variant (Figure 1C-D). Consistently, binding of IGHV3-53/3-66 and IGHV1-2  
73 antibodies to RBD was abolished by either K417N or E484K mutations (Figure S1).

74

75 We next examined all 49 SARS-CoV-2 RBD-targeting antibodies isolated from human  
76 patients with available structures. The epitopes of these antibodies on the RBD can be  
77 classified into six sites: RBS with four subsites RBS-A, B, C, and D; CR3022 site; and  
78 S309 site (Figure S2A). These epitopes assignments are related to the four classes in (44)  
79 (Figure 1C). Sixteen of 18 IGHV3-53/3-66 antibodies target RBS-A, which constitute the  
80 majority of RBS-A antibodies with reported structures (Figure 2A). All IGHV1-2 antibodies  
81 with available structures bind to the RBS-B epitope. A large fraction of the antibodies in  
82 these two main families interact with K417, E484 or N501 (Figure 2A). Almost all RBS-A  
83 antibodies interact extensively with K417 (and N501), whereas E484 is involved in  
84 interactions with most RBS-B and RBS-C antibodies. We also examined the buried  
85 surface area (BSA) of K417, E484, and N501 in the interface of these RBD-targeting  
86 antibodies (Figure S2B). The BSA confirmed why mutations at 417 and 484 affect binding  
87 and neutralization. Although several antibodies interact with N501, especially those  
88 targeting RBS-A, the N501 BSA is 30 Å<sup>2</sup> or less, which is much smaller than the  
89 corresponding interactions with 417 and 484 (Figure S2B) (45). Antibodies targeting the  
90 RBS-D, S309 and CR3022 sites are minimally or not involved in interactions with any of  
91 these three mutated residues (Figure 2A-B).

92

93 Importantly, all of the IGHV3-53/3-66 antibodies that bind to the RBS-A epitope interact  
94 with K417 (and N501Y), consistent with our neutralization results (Figure 1C-D).

95 Previously, we and others demonstrated that IGHV3-53/3-66 RBD antibodies can adopt  
96 two different binding modes (44, 46), which we now refer to as binding modes 1 and 2,  
97 with distinct epitopes and angles of approach to the receptor binding site (RBS) (Figure  
98 2B, Figure S3). All known IGHV3-53/3-66 RBD antibodies with binding mode 1 have a  
99 short CDR H3 of < 15 amino acids and bind to the RBS-A epitope (11, 15, 31), while those  
100 with binding mode 2 contain a longer CDR H3 ( $\geq 15$  amino acids) and target RBS-B (44,  
101 46, 47). These dual binding modes enhance the recognition potential of this antibody  
102 family for the SARS-CoV-2 RBD, although 16 of 18 IGHV3-53/3-66 RBD antibodies with  
103 structural information adopt binding mode 1 (Figure S3). K417 is an important epitope  
104 residue for all 16 antibodies with IGHV3-53/3-66 binding mode 1 (Figure 2B, Figure S3).  
105 IGHV3-53 germline residues V<sub>H</sub> Y33 and Y52 make hydrophobic interactions with the  
106 aliphatic component of K417, and its  $\epsilon$ -amino group interacts with CDR H3 through a salt  
107 bridge (D97 or E97), hydrogen bond, or cation- $\pi$  interactions (F99) (Figure 2B). K417N/T  
108 would diminish such interactions and, therefore, affect antibody binding and neutralization.  
109 This observation provides a structural explanation for K417N escape in all tested IGHV3-  
110 53/3-66 antibodies with binding mode 1 (Figures 1C-D and 2B, Figure S3). In contrast,  
111 IGHV3-53/3-66 antibodies with binding mode 2 do not interact with RBD-K417 (Figure S3),  
112 but with E484. Their CDR H2 hydrogen bonds (H-bond) with E484 through main-chain  
113 and sidechain-mediated H-bond interactions (Figure 2C). Consistently, binding and  
114 neutralization of IGHV3-53/3-66 antibodies with binding mode 2 (Figure S3) are abolished  
115 by E484K, but not K417N (Figure 1C-D, Figure S1).

116

117 Among the IGHV genes used in RBD antibodies, IGHV1-2 is also highly enriched over the  
118 baseline frequency in the antibody repertoire of healthy individuals (48), and is second  
119 only to IGHV3-53/3-66 (Figure 1B). We compared three available structures of IGHV1-2  
120 antibodies, namely 2-4 (26), S2M11 (29), and C121 (44). Similar to IGHV3-53/3-66 RBD

121 antibodies, these IGHV1-2 antibodies also target the RBS, but to RBS-B. Despite being  
122 encoded by different IGK(L)V genes, 2-4 (IGLV2-8), S2M11 (IGKV3-20), and C121  
123 (IGLV2-23) share a nearly identical binding mode and epitope (Figure 3A). Structural  
124 analysis reveals that the  $V_H$  <sup>26</sup>GTFTG(Y)Y<sup>33</sup>, <sup>50</sup>W(I)N/S(P)XSXGTX<sup>58</sup>, <sup>73</sup>TS(I)S/T<sup>76</sup> motifs  
125 are important for RBD binding (Figure S4A-D). Although only a small area of the epitope  
126 is conferred by the light chains of 2-4, S2M11, and C121,  $V_L$  residues 32 and 91 (n.b. also  
127 residue 30 for some antibodies) play an important role in forming a hydrophobic pocket  
128 together with  $V_H$  residues for binding RBD-F486, which we consider another key binding  
129 residue in such classes of antibodies (46) (Figure S4E-I). A recent study also showed that  
130 three other IGHV1-2 antibodies, 2-43, 2-15, and H4 bind in a similar mode, further  
131 highlighting structural convergence of IGHV1-2 antibodies in targeting the same RBD  
132 epitope (49). Importantly, all IGHV1-2 antibodies to date form extensive interactions with  
133 E484 (Figure 3A, Figure S2B). In particular, germline-encoded  $V_H$  Y33 and  $V_H$  N52  
134 (somatically mutated to S52 in C121) and S54 are involved in polar interactions with the  
135 side chain of RBD-E484, where these H-bonds would be altered by substitution with Lys  
136 (Figure 3A) and diminish binding and neutralization of IGHV1-2 antibodies against E484K  
137 (Figure 1C-D, Figure S1). Consistent with the neutralization results, E484 has a large BSA  
138 when complexed with these antibodies (Figure S2B)

139

140 We previously isolated another IGHV1-2 antibody, CV05-163, from a COVID-19 patient  
141 (16). Interestingly, CV05-163 has no somatic mutations, and binds to SARS-CoV-2 RBD  
142 with a  $K_D$  of 0.2 nM as an IgG (16) and 45.3 nM as a Fab (Figure S5). CV05-163 also  
143 exhibited high neutralization potency with an  $IC_{50}$  of 16.3 ng/ml against authentic SARS-  
144 CoV-2 (16). Negative-stain electron microscopy (nsEM) of CV05-163 in complex with the  
145 SARS-CoV-2 S trimer illustrated that this antibody binds in various stoichiometries,  
146 including molar ratios of 1:1, 2:1, and 3:1 (Fab to S protein trimer), where RBDs in both

147 up- and down-conformations can be accommodated by CV05-163 (Figure S6). We also  
148 determined a crystal structure of Fab CV05-163 in complex with SARS-CoV-2 RBD and  
149 Fab CR3022 to 2.25 Å resolution (Figure 3B, Figure S7, Tables S1 and S2) and show that  
150 it also binds to RBS-B. However, the binding orientation of Fab CV05-163 to the RBD  
151 (Figure 3B) is rotated 90° compared to other IGHV1-2 RBD antibodies 2-4, S2M11, and  
152 C121 (Figure 3A). CDR H2 forms three H-bonds as well as hydrophobic interactions with  
153 the RBD (Figure S7E). The non-templated nucleotide (N) additions in CDR H3 encode an  
154 <sup>100a</sup>ALPPY<sup>100e</sup> motif (Figures S7F and S8) that makes a major contribution to the RBD-  
155 interactions and promotes aromatic interactions between V<sub>L</sub> Y32 and V<sub>L</sub> Y49 and the RBD  
156 (Figure S9). All paratope residues on the light chain are encoded by IGKV3-11 (Figure  
157 S8), which form nine H-bonds and salt bridges as well as multiple hydrophobic interactions  
158 (Figure S7G-I). Of note, CV05-163 likely represents a public clonotype for IGHV1-2 RBD  
159 antibodies across patients (Figure S10). In contrast to the other IGHV1-2 antibodies with  
160 a canonical binding mode (2-4, S2M11, and C121) where four residues stack with RBD-  
161 F486, CV05-163 in this alternate binding mode interacts with RBD-F486 via only one  
162 residue (Figure S4E-G). Nevertheless, CV05-163 binds to a similar epitope as the other  
163 IGHV1-2 RBD antibodies (Figure 3). Importantly, CV05-163 also extensively interacts with  
164 RBD-E484 via H-bonds (V<sub>H</sub> W50 and V<sub>H</sub> N58) and a salt bridge (V<sub>L</sub> R91) (Figure 3B) that  
165 explains why the binding and neutralization by CV05-163 were diminished by the E484K  
166 mutant (Figure 1C-D, Figure S1). As a result, IGHV1-2 antibodies [like IGHV3-53/66 (47)],  
167 can also engage the RBD in another example of two different binding modes, both of which  
168 are susceptible to escape by the E484K mutation, but not K417N (Figure 1C-D).

169

170 A further group of antibodies target the back side of the RBS on the opposite side of the  
171 RBS ridge (called RBS-C) (46). To date, structures of five antibodies isolated from COVID-  
172 19 patients can be classified as binding to the RBS-C epitope: CV07-270 (16), BD-368-2

173 (37), P2B-2F6 (17), C104 (44), and P17 (50). All of these RBS-C antibodies also interact  
174 with E484 (Figure 4A), many with an Arg residue in CDR H3, suggesting that RBD-E484K  
175 may influence neutralization by RBS-C antibodies. Indeed, binding and neutralization of  
176 RBS-C antibody CV07-270 was abrogated by RBD-E484K (Figure S1 and Figure 1C).  
177 Intriguingly, the five RBS-C antibodies with solved structures are encoded by five different  
178 IGHV genes, but target a similar epitope with similar angles of approach. Furthermore,  
179 SARS-CoV-2 pseudovirus neutralization by two other highly potent antibodies CC6.29 (12)  
180 and COVA2-15 (19) was markedly reduced by the E484K mutation (Figure 1C). In addition,  
181 neutralization by REGN10933 was reduced by both K417N and E484K (Figure 1C), which  
182 is a potent antibody used for the therapeutic treatment of COVID-19 (27). REGN10933  
183 has a slightly different angle of binding from RBS-A antibodies and tilts slightly towards  
184 RBS-B. Thus, K417 can interact with CDRs H1 and H3 of REGN10933, whereas E484  
185 makes contacts with CDR H2 (Figure S11). Overall, our results demonstrate that RBS  
186 mutations K417N and E484K can either abolish or extensively reduce the binding and  
187 neutralization of several major classes of SARS-CoV-2 RBD antibodies.

188

189 Two other non-RBS sites that are distant from K417 and E484 have been repeatedly  
190 reported to be neutralizing sites on the SARS-CoV-2 RBD, namely the CR3022 cryptic  
191 site and S309 proteoglycan site (46) (Figures 1C and 4B). We and others have previously  
192 shown that antibodies from COVID-19 patients can neutralize SARS-CoV-2 by targeting  
193 the CR3022 site, including COVA1-16 (51), S304, S2A4 (30), and DH1047 (40). Recently,  
194 we found that CV38-142 also targets the S309 site (52). Antibodies targeting these two  
195 sites are often cross-reactive with other sarbecoviruses, since these sites are more  
196 evolutionarily conserved compared to the RBS. To test the effect of the RBD-K417N and  
197 RBD-E484K mutations on neutralizing antibodies that target the S309 and CR3022 sites,  
198 we performed binding and neutralization assays on CV38-142 and COVA1-16. Both

199 mutations have minimal effect on these antibodies (Figures 1C and 4C). In fact, recent  
200 studies have shown that sera from convalescent or vaccinated individuals can retain  
201 neutralization activity, albeit reduced, against the mutated variants (7, 9, 53), suggesting  
202 that antibodies targeting other epitopes including CR3022 and S309 sites, as well as the  
203 NTD, are also present. Thus, the CR3022 cryptic site and S309 site are promising targets  
204 to avoid interference by SARS-CoV-2 mutations observed to date.

205

206 As SARS-CoV-2 continues to circulate in humans and increasing numbers of COVID-19  
207 vaccines are administered, herd immunity to SARS-CoV-2 is gradually building up both  
208 locally and globally. However, as with other RNA viruses, such as influenza and HIV (54),  
209 further antigenic drift is anticipated in SARS-CoV-2. Such antigenic drift was also observed  
210 in at least one well-studied immunosuppressed COVID-19 patient, and included N501Y  
211 and E484K mutations (55). A recent study also showed the ability of seasonal  
212 coronaviruses to undergo antigenic drift (56). While antibody responses to the original  
213 lineage that initiated COVID-19 pandemic are well characterized in many studies (12-17,  
214 19, 22, 25, 26, 28), it is unclear at present how similar the antibody response would be to  
215 antigenically distinct lineages. It is possible that IGHV3-53 and IGHV1-2 will not be as  
216 enriched in response to infection by the B.1.351 and B.1.1.28.1 lineages or would require  
217 greater SHM over the low level reported so far. These questions therefore require urgent  
218 attention. Moreover, ongoing efforts to evaluate antibody responses and escape is  
219 essential for development and/or modification of COVID-19 vaccines.

220

221 In the emerging SARS-CoV-2 lineages, several mutations alter the antigenicity of the RBD  
222 as well as the NTD (57). While a polyclonal response is generated by natural infection and  
223 vaccination, the neutralizing immune response seems to be biased towards particular  
224 epitopes and antibody germ lines. Many SARS-CoV-2 neutralizing antibodies target the

225 RBS on the RBD, where the most frequent and enriched antibodies are focused on three  
226 different sub-epitopes on the RBS. The three most frequent classes (RBS-A, B, C) are  
227 adversely affected by mutations at positions 417 and 484 in the South Africa and Brazil  
228 lineages. Notwithstanding, some variation in response to these residues from person to  
229 person will depend on the characteristics of individual immune responses. However, the  
230 epitopes for cross-reactive neutralizing antibodies to the RBD generally do not overlap  
231 with the RBS sites. Thus, cross-reactive neutralizing antibodies have not only the potential  
232 to confer protection against other zoonotic sarbecoviruses with pandemic potential, but  
233 also against antigenically drifted SARS-CoV-2 variants (58, 59). As SARS-CoV-2 is likely  
234 to become endemic (60), it is time to fast track to more broadly effective vaccines and  
235 therapeutics that are more resistant to antigenic variation.



## 236 REFERENCES

- 237 1. H. Tegally *et al.*, Emergence and rapid spread of a new severe acute respiratory  
238 syndrome-related coronavirus 2 (SARS-CoV-2) lineage with multiple spike  
239 mutations in South Africa. *medRxiv* 10.1101/2020.12.21.20248640, (2020).
- 240 2. N. R. Faria *et al.*, Genomic characterisation of an emergent SARS-CoV-2 lineage  
241 in Manaus: preliminary findings. [https://virological.org/t/genomic-characterisation-](https://virological.org/t/genomic-characterisation-of-an-emergent-sars-cov-2-lineage-in-manaus-preliminary-findings/586)  
242 [of-an-emergent-sars-cov-2-lineage-in-manaus-preliminary-findings/586](https://virological.org/t/genomic-characterisation-of-an-emergent-sars-cov-2-lineage-in-manaus-preliminary-findings/586), (2021).
- 243 3. Public Health England, *Investigation of novel SARS-CoV-2 variant: 202012/01.*  
244 *Technical briefing 5* (2021).
- 245 4. Y. Weisblum *et al.*, Escape from neutralizing antibodies by SARS-CoV-2 spike  
246 protein variants. *eLife* **9**, e61312 (2020).
- 247 5. A. J. Greaney *et al.*, Complete mapping of mutations to the SARS-CoV-2 spike  
248 receptor-binding domain that escape antibody recognition. *Cell Host Microbe* **29**,  
249 44-57.e49 (2021).
- 250 6. E. Andreano *et al.*, SARS-CoV-2 escape *in vitro* from a highly neutralizing  
251 COVID-19 convalescent plasma. *bioRxiv* 10.1101/2020.12.28.424451, (2020).
- 252 7. C. K. Wibmer *et al.*, SARS-CoV-2 501Y.V2 escapes neutralization by South  
253 African COVID-19 donor plasma. *bioRxiv* 10.1101/2021.01.18.427166, (2021).
- 254 8. A. J. Greaney *et al.*, Comprehensive mapping of mutations to the SARS-CoV-2  
255 receptor-binding domain that affect recognition by polyclonal human serum  
256 antibodies. *bioRxiv* 10.1101/2020.12.31.425021, (2021).
- 257 9. Z. Wang *et al.*, mRNA vaccine-elicited antibodies to SARS-CoV-2 and circulating  
258 variants. *Nature* 10.1038/s41586-021-03324-6, (2021).
- 259 10. L. Stamatatos *et al.*, Antibodies elicited by SARS-CoV-2 infection and boosted by  
260 vaccination neutralize an emerging variant and SARS-CoV-1. *medRxiv*  
261 10.1101/2021.02.05.21251182, (2021).
- 262 11. M. Yuan *et al.*, Structural basis of a shared antibody response to SARS-CoV-2.  
263 *Science* **369**, 1119-1123 (2020).
- 264 12. T. F. Rogers *et al.*, Isolation of potent SARS-CoV-2 neutralizing antibodies and  
265 protection from disease in a small animal model. *Science* **369**, 956-963 (2020).
- 266 13. Y. Cao *et al.*, Potent neutralizing antibodies against SARS-CoV-2 identified by  
267 high-throughput single-cell sequencing of convalescent patients' B cells. *Cell*  
268 **182**, 73-84 e16 (2020).
- 269 14. D. F. Robbiani *et al.*, Convergent antibody responses to SARS-CoV-2 in  
270 convalescent individuals. *Nature* **584**, 437-442 (2020).



- 271 15. C. O. Barnes *et al.*, Structures of human antibodies bound to SARS-CoV-2 spike  
272 reveal common epitopes and recurrent features of antibodies. *Cell* **182**, 828-842  
273 e816 (2020).
- 274 16. J. Kreye *et al.*, A therapeutic non-self-reactive SARS-CoV-2 antibody protects  
275 from lung pathology in a COVID-19 hamster model. *Cell* **183**, 1058-1069.e1019  
276 (2020).
- 277 17. B. Ju *et al.*, Potent human neutralizing antibodies elicited by SARS-CoV-2  
278 infection. *bioRxiv* 10.1101/2020.03.21.990770, (2020).
- 279 18. D. Pinto *et al.*, Cross-neutralization of SARS-CoV-2 by a human monoclonal  
280 SARS-CoV antibody. *Nature* **583**, 290-295 (2020).
- 281 19. P. J. M. Brouwer *et al.*, Potent neutralizing antibodies from COVID-19 patients  
282 define multiple targets of vulnerability. *Science* **369**, 643-650 (2020).
- 283 20. Y. Wu *et al.*, A noncompeting pair of human neutralizing antibodies block COVID-  
284 19 virus binding to its receptor ACE2. *Science* **368**, 1274-1278 (2020).
- 285 21. X. Chi *et al.*, A neutralizing human antibody binds to the N-terminal domain of the  
286 Spike protein of SARS-CoV-2. *Science* **369**, 650-655 (2020).
- 287 22. E. Seydoux *et al.*, Analysis of a SARS-CoV-2-infected individual reveals  
288 development of potent neutralizing antibodies with limited somatic mutation.  
289 *Immunity* **53**, 98-105 e105 (2020).
- 290 23. R. Shi *et al.*, A human neutralizing antibody targets the receptor-binding site of  
291 SARS-CoV-2. *Nature* **584**, 120-124 (2020).
- 292 24. X. Han *et al.*, A rapid and efficient screening system for neutralizing antibodies  
293 and its application for the discovery of potent neutralizing antibodies to SARS-  
294 CoV-2 S-RBD. *bioRxiv* 10.1101/2020.08.19.253369, (2020).
- 295 25. S. J. Zost *et al.*, Rapid isolation and profiling of a diverse panel of human  
296 monoclonal antibodies targeting the SARS-CoV-2 spike protein. *Nat Med* **26**,  
297 1422-1427 (2020).
- 298 26. L. Liu *et al.*, Potent neutralizing antibodies against multiple epitopes on SARS-  
299 CoV-2 spike. *Nature* **584**, 450-456 (2020).
- 300 27. J. Hansen *et al.*, Studies in humanized mice and convalescent humans yield a  
301 SARS-CoV-2 antibody cocktail. *Science* **369**, 1010-1014 (2020).
- 302 28. C. Kreer *et al.*, Longitudinal isolation of potent near-germline SARS-CoV-2-  
303 neutralizing antibodies from COVID-19 patients. *Cell* **182**, 843-854 e812 (2020).
- 304 29. M. A. Tortorici *et al.*, Ultrapotent human antibodies protect against SARS-CoV-2  
305 challenge via multiple mechanisms. *Science* **370**, 950-957 (2020).

- 306 30. L. Piccoli *et al.*, Mapping neutralizing and immunodominant sites on the SARS-  
307 CoV-2 spike receptor-binding domain by structure-guided high-resolution  
308 serology. *Cell* **183**, 1024-1042.e1021 (2020).
- 309 31. S. A. Clark *et al.*, Molecular basis for a germline-biased neutralizing antibody  
310 response to SARS-CoV-2. *bioRxiv* 10.1101/2020.11.13.381533, (2020).
- 311 32. M. Mor *et al.*, Multi-clonal live SARS-CoV-2 in vitro neutralization by antibodies  
312 isolated from severe COVID-19 convalescent donors. *bioRxiv*  
313 10.1101/2020.10.06.323634, (2020).
- 314 33. R. Babb *et al.* (Regeneron Pharmaceuticals, Inc., 2020), vol. B1, chap.  
315 US10787501.
- 316 34. M. Yuan *et al.*, A highly conserved cryptic epitope in the receptor binding  
317 domains of SARS-CoV-2 and SARS-CoV. *Science* **368**, 630-633 (2020).
- 318 35. N. K. Hurlburt *et al.*, Structural basis for potent neutralization of SARS-CoV-2 and  
319 role of antibody affinity maturation. *Nat Commun* **11**, 5413 (2020).
- 320 36. T. Noy-Porat *et al.*, A panel of human neutralizing mAbs targeting SARS-CoV-2  
321 spike at multiple epitopes. *Nat Commun* **11**, 4303 (2020).
- 322 37. S. Du *et al.*, Structurally resolved SARS-CoV-2 antibody shows high efficacy in  
323 severely infected hamsters and provides a potent cocktail pairing strategy. *Cell*  
324 **183**, 1013–1023.e1013 (2020).
- 325 38. Y. Zhou *et al.*, Enhancement versus neutralization by SARS-CoV-2 antibodies  
326 from a convalescent donor associates with distinct epitopes on the RBD. *Cell*  
327 *Rep* 10.1016/j.celrep.2021.108699, 108699 (2021).
- 328 39. A. R. Shiakolas *et al.*, Cross-reactive coronavirus antibodies with diverse epitope  
329 specificities and extra-neutralization functions. *bioRxiv*  
330 10.1101/2020.12.20.414748, (2020).
- 331 40. D. Li *et al.*, The functions of SARS-CoV-2 neutralizing and infection-enhancing  
332 antibodies in vitro and in mice and nonhuman primates. *bioRxiv*  
333 10.1101/2020.12.31.424729, (2021).
- 334 41. B. B. Banach *et al.*, Paired heavy and light chain signatures contribute to potent  
335 SARS-CoV-2 neutralization in public antibody responses. *bioRxiv*  
336 10.1101/2020.12.31.424987, (2021).
- 337 42. G. Bullen *et al.*, Deep mining of early antibody response in COVID-19 patients  
338 yields potent neutralisers and reveals high level of convergence. *bioRxiv*  
339 10.1101/2020.12.29.424711, (2020).
- 340 43. J. Wan *et al.*, Human-IgG-neutralizing monoclonal antibodies block the SARS-  
341 CoV-2 infection. *Cell Rep* **32**, 107918 (2020).

- 342 44. C. O. Barnes *et al.*, SARS-CoV-2 neutralizing antibody structures inform  
343 therapeutic strategies. *Nature* **588**, 682–687 (2020).
- 344 45. X. Xie *et al.*, Neutralization of N501Y mutant SARS-CoV-2 by BNT162b2  
345 vaccine-elicited sera. *bioRxiv* 10.1101/2021.01.07.425740,  
346 2021.2001.2007.425740 (2021).
- 347 46. M. Yuan, H. Liu, N. C. Wu, I. A. Wilson, Recognition of the SARS-CoV-2 receptor  
348 binding domain by neutralizing antibodies. *Biochem Biophys Res Commun*  
349 10.1016/j.bbrc.2020.10.012, (2020).
- 350 47. N. C. Wu *et al.*, An alternative binding mode of IGHV3-53 antibodies to the  
351 SARS-CoV-2 receptor binding domain. *Cell Rep* **33**, 108274 (2020).
- 352 48. S. D. Boyd *et al.*, Individual variation in the germline Ig gene repertoire inferred  
353 from variable region gene rearrangements. *J Immunol* **184**, 6986-6992 (2010).
- 354 49. M. Rapp *et al.*, Modular basis for potent SARS-CoV-2 neutralization by a  
355 prevalent VH1-2-derived antibody class. *bioRxiv* 10.1101/2021.01.11.426218,  
356 (2021).
- 357 50. H. Yao *et al.*, Rational development of a human antibody cocktail that deploys  
358 multiple functions to confer Pan-SARS-CoVs protection. *Cell Res* **31**, 25-36  
359 (2021).
- 360 51. H. Liu *et al.*, Cross-neutralization of a SARS-CoV-2 antibody to a functionally  
361 conserved site is mediated by avidity. *Immunity* **53**, 1272-1280.e1275 (2020).
- 362 52. H. Liu *et al.*, A combination of cross-neutralizing antibodies synergizes to prevent  
363 SARS-CoV-2 and SARS-CoV pseudovirus infection. *bioRxiv*  
364 10.1101/2021.02.11.430866, (2021).
- 365 53. K. Wu *et al.*, mRNA-1273 vaccine induces neutralizing antibodies against spike  
366 mutants from global SARS-CoV-2 variants. *bioRxiv* 10.1101/2021.01.25.427948,  
367 (2021).
- 368 54. G. B. Karlsson Hedestam *et al.*, The challenges of eliciting neutralizing  
369 antibodies to HIV-1 and to influenza virus. *Nat Rev Microbiol* **6**, 143-155 (2008).
- 370 55. B. Choi *et al.*, Persistence and Evolution of SARS-CoV-2 in an  
371 Immunocompromised Host. *N Engl J Med* **383**, 2291-2293 (2020).
- 372 56. R. Eguia *et al.*, A human coronavirus evolves antigenically to escape antibody  
373 immunity. *bioRxiv* 10.1101/2020.12.17.423313, (2020).
- 374 57. P. Wang *et al.*, Increased resistance of SARS-CoV-2 variants B.1.351 and  
375 B.1.1.7 to antibody neutralization. *bioRxiv* 10.1101/2021.01.25.428137, (2021).
- 376 58. V. D. Menachery *et al.*, A SARS-like cluster of circulating bat coronaviruses  
377 shows potential for human emergence. *Nat Med* **21**, 1508-1513 (2015).

- 378 59. V. D. Menachery *et al.*, SARS-like WIV1-CoV poised for human emergence. *Proc*  
379 *Natl Acad Sci U S A* **113**, 3048-3053 (2016).
- 380 60. S. M. Kissler, C. Tedijanto, E. Goldstein, Y. H. Grad, M. Lipsitch, Projecting the  
381 transmission dynamics of SARS-CoV-2 through the postpandemic period.  
382 *Science* **368**, 860-868 (2020).
- 383 61. J. Lan *et al.*, Structure of the SARS-CoV-2 spike receptor-binding domain bound  
384 to the ACE2 receptor. *Nature* **581**, 215-220 (2020).

385

## 386 **ACKNOWLEDGEMENTS**

387 We thank Henry Tien for technical support with the crystallization robot, Jeanne Matteson  
388 and Yuanzi Hua for their contributions to mammalian cell culture, Wenli Yu to insect cell  
389 culture, and Robyn Stanfield for assistance in data collection. This work was supported by  
390 the Bill and Melinda Gates Foundation OPP1170236 and INV-004923 INV (I.A.W., A.B.W.,  
391 D.R.B.), NIH R00 AI139445 (N.C.W.), R01 AI132317 (D.N. and D.H.), R01 AI142945  
392 (L.P.), and by the German Research Foundation (H.P.). R.W.S. is a recipient of a Vici  
393 fellowship from the Netherlands Organisation for Scientific Research (NWO). This  
394 research used resources of the Advanced Photon Source, a U.S. Department of Energy  
395 (DOE) Office of Science User Facility, operated for the DOE Office of Science by Argonne  
396 National Laboratory under Contract No. DE-AC02-06CH11357. Extraordinary facility  
397 operations were supported in part by the DOE Office of Science through the National  
398 Virtual Biotechnology Laboratory, a consortium of DOE national laboratories focused on  
399 the response to COVID-19, with funding provided by the Coronavirus CARES Act.

400

## 401 **AUTHOR CONTRIBUTIONS**

402 M.Y., D.H., C.C.D.L., N.C.W., and I.A.W. conceived and designed the study. M.Y.,  
403 C.C.D.L., N.C.W. and H.L. expressed and purified the proteins for crystallization. S.M.R.,  
404 H.P., and J.K. provided CV05-163 and other antibody clones and sequences. M.J.v.G.

405 and R.W.S, and D.R.B provided plasmids for some of the antibodies reported in (12, 19),  
406 respectively. M.Y. and X.Z. performed the crystallization, X-ray data collection, determined  
407 and refined the X-ray structures. D.H., L.P. and D.N. performed the neutralization assays.  
408 A.M.J., and A.B.W. provided nsEM data and performed reconstructions. M.Y., C.C.D.L.,  
409 N.C.W. and I.A.W. wrote the paper and all authors reviewed and/or edited the paper.

410

#### 411 **COMPETING INTERESTS**

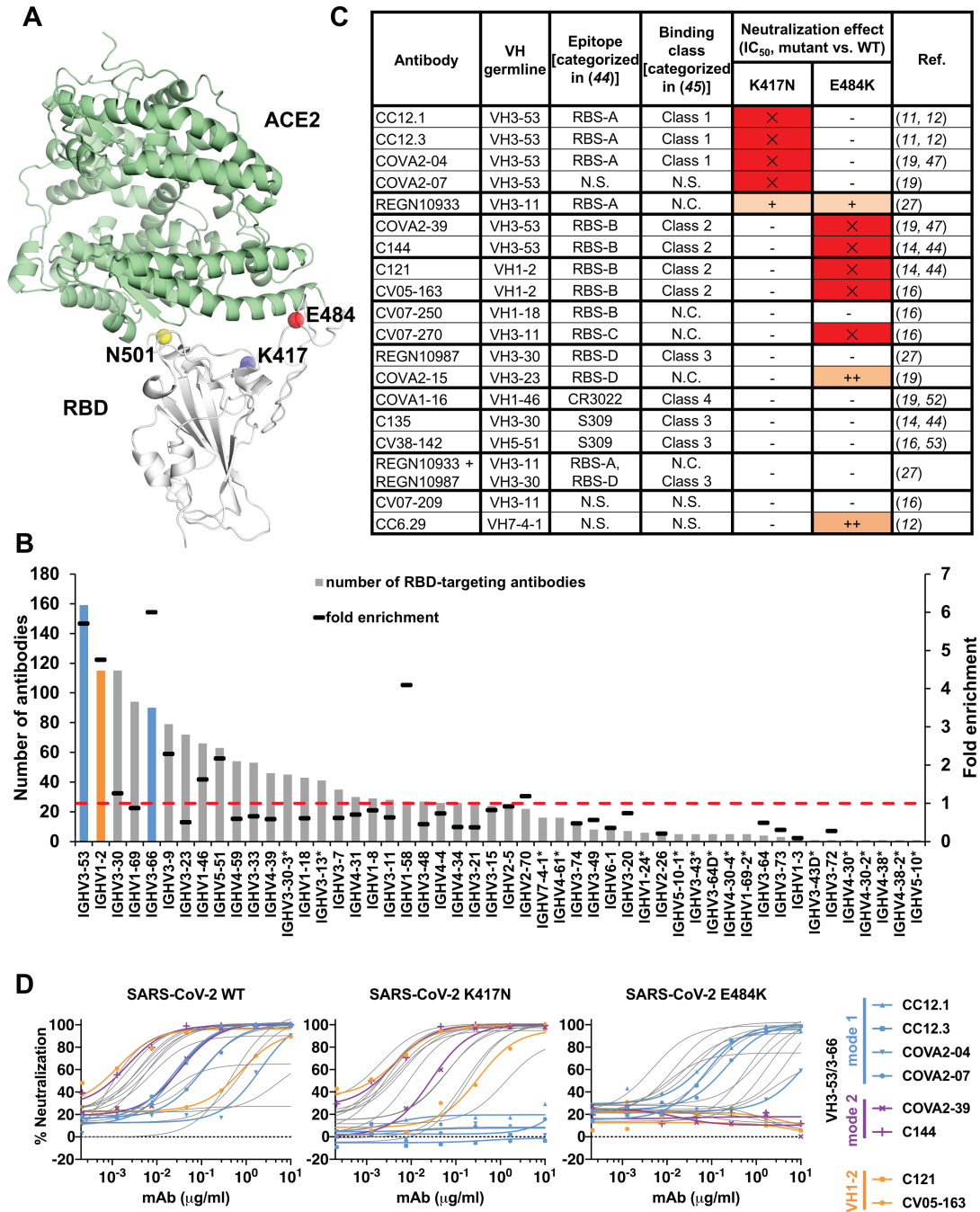
412 Related to this work, the German Center for Neurodegenerative Diseases (DZNE) and  
413 Charité – Universitätsmedizin Berlin previously filed a patent application that included anti-  
414 SARS-CoV-2 antibody CV05-163 first reported in (16).

415

#### 416 **STRUCTURE DEPOSITIONS**

417 The X-ray coordinates and structure factors have been deposited to the RCSB Protein  
418 Data Bank under accession code: 7LOP. The EM maps have been deposited in the  
419 Electron Microscopy Data Bank (EMDB) under accession codes: EMD-23466 (one  
420 bound), EMD-23467 (two bound), and EMD-23468 (three bound).

421



422

423 **Figure 1. Emergent SARS-CoV-2 variants escape two major classes of neutralizing**

424 **antibodies. (A)** Emergent mutations (spheres) in the RBS of B.1.351 and B.1.1.28.1

425 lineages are mapped onto a structure of SARS-CoV-2 RBD (white) in complex with ACE2

426 (green) (PDB ID: 6M0J) (61). **(B)** Distribution of IGHV gene usage. The IGHV gene usage

427 in 1,593 SARS-CoV-2 RBD-targeting antibodies (12-43) compared to healthy individuals

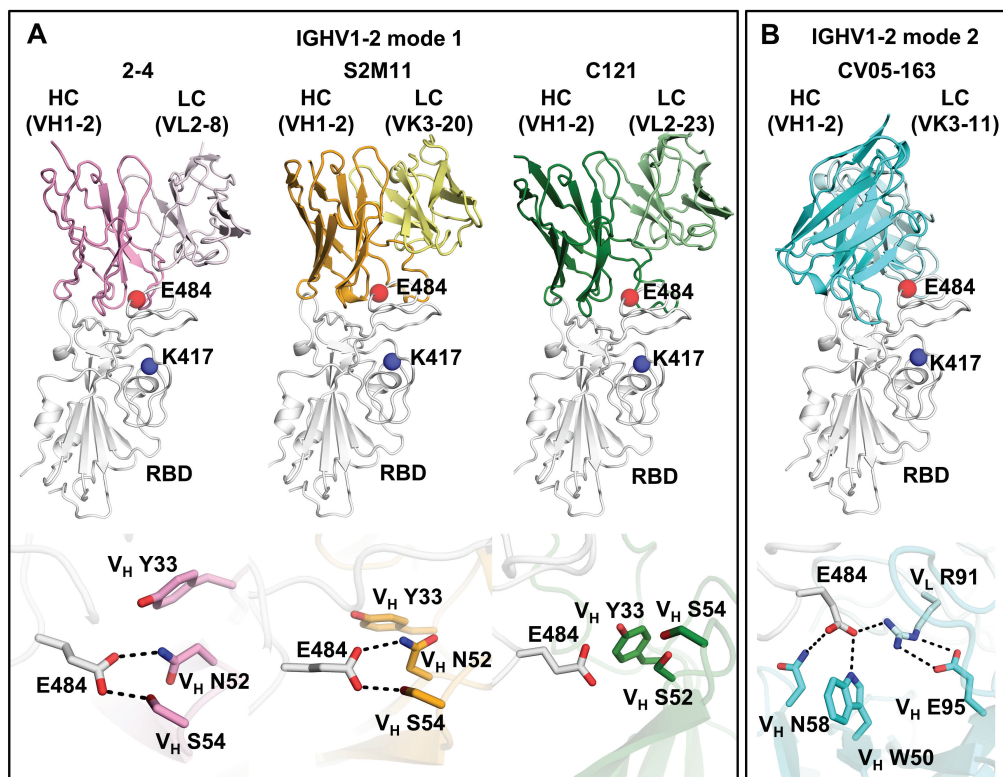
428 (baseline) (48) is shown as bars. IGHV gene frequencies in healthy individuals that were  
429 not reported in (48) are shown with asterisks (\*). Fold-enrichment of germlines used in  
430 SARS-CoV-2 antibodies over baseline is shown as black lines. A fold enrichment of one  
431 (red dashed line) represents no difference over baseline. The frequently used IGHV3-53  
432 and IGHV3-66 genes are highlighted in blue, and IGHV1-2 in orange. Numbers of RBD-  
433 targeting antibodies encoded by each IGHV gene is shown as black lines. **(C)** Effect of  
434 single mutations on the neutralization activity of each neutralizing antibody. IC<sub>50</sub> increases  
435 that are less than 10-fold are represented by “-”, between 10- and 100-fold as “+”, and  
436 greater than 100-fold as “++”. Results in red with “X” indicate no neutralization activity was  
437 detected at 10 µg/ml of IgG. N.C.: not categorized in the original studies. N.S.: No structure  
438 available. **(D)** Neutralization of pseudotyped SARS-CoV-2 virus and variants carrying  
439 K417N or E484K mutations. A panel of 18 neutralizing antibodies were tested, including  
440 four mode-1 IGHV3-53 antibodies (blue), two mode-2 IGHV3-53 antibodies (purple), and  
441 two IGHV1-2 antibodies (orange).  
442





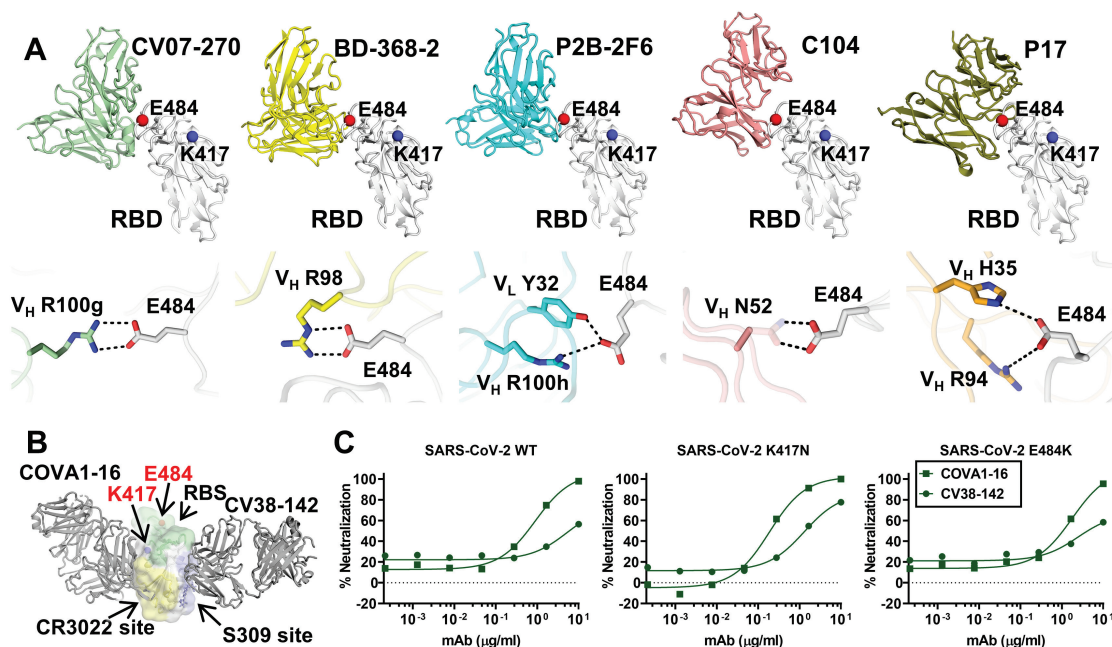


454 6XC3), CC12.3 (PDB ID: 6XC4) (11), and COVA2-04 (PDB ID: 7JMO) (47)] and **(C)**  
455 binding mode 2 [COVA2-39 (PDB ID: 7JMP) (47)]. The SARS-CoV-2 RBD is in white and  
456 Fabs in different colors. Residues K417 and E484 are represented by blue and red  
457 spheres, respectively. Hydrogen bonds and salt bridges are represented by black dashed  
458 lines.



459

460 **Figure 3. E484 is critical for RBD recognition of IGHV1-2 antibodies.** Heavy and light  
461 chains of antibody 2-4 (PDB 6XEY) (26) are shown in pink and light pink, respectively,  
462 S2M11 (PDB 7K43) (29) in orange and yellow, and C121 (PDB 7K8X) (44) in dark and  
463 light green, and CV05-163 in cyan and light cyan. The RBD is shown in white. E484 and  
464 K417 are highlighted as red and blue spheres, respectively. Hydrogen bonds are  
465 represented by dashed lines. Hydrogen bonds are not shown in the panel of C121 due to  
466 the limited resolution (3.9 Å).



467

468 **Figure 4. Antibodies targeting other major antigenic sites are differentially affected**

469 **by mutations in recent variants. (A)** Interactions between RBS-C antibodies and SARS-

470 CoV-2 RBD. The RBD is shown in white with E484, K417 represented as red and blue

471 spheres, respectively. The various antibodies illustrated are in different colors. Only the

472 variable domains are shown for clarity. Hydrogen bonds and salt bridges to E484 are

473 represented by dashed lines. Published structures with PDB IDs 6XKP (16), 7CHF (37),

474 7BWJ (17), 7K8U (44), and 7CWN (50) are used to depict structures of SARS-CoV-2 RBD

475 with CV07-270, BD-368-2, P2B-2F6, C104, and P17, respectively. The electron density

476 for the full side chain of V<sub>H</sub> N52 was not well resolved in the 3.8-Å structure of C104 in

477 complex with SARS-CoV-2 S. The full side chain is modeled here and shown as

478 transparent sticks to illustrate a possible interaction with E484. **(B)** Cross-neutralizing

479 antibodies to the RBD are not affected by E484 and K417 mutations. COVA1-16 targets

480 the CR3022 cryptic site (yellow) (51) and CV38-142 targets the S309 proteoglycan site

481 (blue) (52) to the RBD. Glycans at the N343 glycosylation site are represented by sticks.

482 The RBS surface is shown in green. E484 and K417 are highlighted as red and blue

483 spheres, respectively. **(C)** Neutralization of CV38-142 and COVA1-16 against SARS-CoV-  
484 2 wild type, K417N or E484K pseudoviruses.

## 485 **MATERIALS AND METHODS**

### 486 **Expression and purification of SARS-CoV-2 RBD**

487 Expression and purification of the SARS-CoV-2 spike receptor-binding domain (RBD)  
488 were as described previously (1). Briefly, the RBD (residues 319-541) of the SARS-CoV-  
489 2 spike (S) protein (GenBank: QHD43416.1) was cloned into a customized pFastBac  
490 vector (2), and fused with an N-terminal gp67 signal peptide and C-terminal His<sub>6</sub> tag (1).  
491 A recombinant bacmid DNA was generated using the Bac-to-Bac system (Life  
492 Technologies). Baculovirus was generated by transfecting purified bacmid DNA into Sf9  
493 cells using FuGENE HD (Promega), and subsequently used to infect suspension cultures  
494 of High Five cells (Life Technologies) at an MOI of 5 to 10. Infected High Five cells were  
495 incubated at 28 °C with shaking at 110 r.p.m. for 72 h for protein expression. The  
496 supernatant was then concentrated using a 10 kDa MW cutoff Centrimate cassette (Pall  
497 Corporation). The RBD protein was purified by Ni-NTA, followed by size exclusion  
498 chromatography, and buffer exchanged into 20 mM Tris-HCl pH 7.4 and 150 mM NaCl.

499

### 500 **Expression and purification of Fabs**

501 The heavy and light chains were cloned into pHCMV3. The plasmids were transiently co-  
502 transfected into ExpiCHO cells at a ratio of 2:1 (HC:LC) using ExpiFectamine™ CHO  
503 Reagent (Thermo Fisher Scientific) according to the manufacturer's instructions. The  
504 supernatant was collected at 10 days post-transfection. The Fabs were purified with a  
505 CaptureSelect™ CH1-XL Affinity Matrix (Thermo Fisher Scientific) followed by size  
506 exclusion chromatography.

507

### 508 **Crystallization and structural determination**

509 A complex of CV05-163 with RBD and CR3022 was formed by mixing each of the protein  
510 components at an equimolar ratio and incubating overnight at 4°C. The protein complex

511 was adjusted to 12 mg/ml and screened for crystallization using the 384 conditions of the  
512 JCSG Core Suite (Qiagen) on our robotic CrystalMation system (Rigaku) at Scripps  
513 Research. Crystallization trials were set-up by the vapor diffusion method in sitting drops  
514 containing 0.1  $\mu$ l of protein and 0.1  $\mu$ l of reservoir solution. Optimized crystals were then  
515 grown in drops containing 0.1 M sodium citrate – citric acid buffer at pH 4.8 and 19% (w/v)  
516 polyethylene glycol 6000 at 20°C. Crystals appeared on day 3, were harvested on day 7  
517 by soaking in reservoir solution supplemented with 15% (v/v) ethylene glycol, and then  
518 flash cooled and stored in liquid nitrogen until data collection. Diffraction data were  
519 collected at cryogenic temperature (100 K) at beamline 23-ID-B of the Advanced Photon  
520 Source (APS) at Argonne National Labs with a beam wavelength of 1.033 Å, and  
521 processed with HKL2000 (3). Structures were solved by molecular replacement using  
522 PHASER (4). Models for molecular replacement of the RBD and CR3022 were derived  
523 from PDB 6W41 (1), whereas a model of CV05-163 was generated by Repertoire Builder  
524 ([https://sysimm.ifrec.osaka-u.ac.jp/rep\\_builder/](https://sysimm.ifrec.osaka-u.ac.jp/rep_builder/)) (5). Iterative model building and  
525 refinement were carried out in COOT (6) and PHENIX (7), respectively. Epitope and  
526 paratope residues, as well as their interactions, were identified by accessing PISA at the  
527 European Bioinformatics Institute ([http://www.ebi.ac.uk/pdbe/prot\\_int/pistart.html](http://www.ebi.ac.uk/pdbe/prot_int/pistart.html)) (8).

528

### 529 **Biolayer interferometry binding assay**

530 Binding assays were performed by biolayer interferometry (BLI) using an Octet Red  
531 instrument (FortéBio) as described previously (1). To measure the binding kinetics of anti-  
532 SARS-CoV-2 IgGs and RBDs (wild type and K417N and E484K variants), the IgGs were  
533 diluted with kinetic buffer (1x PBS, pH 7.4, 0.01% BSA and 0.002% Tween 20) into 30  
534  $\mu$ g/ml. IgG cocktail of two antibodies REGN10933 and REGN10987 were prepared in  
535 equimolar ratios of each IgG in 30  $\mu$ g/ml. The IgGs were then loaded onto anti-human IgG  
536 Fc (AHC) biosensors and interacted with 30  $\mu$ g/ml wild type, K417N, and E484K SARS-

537 CoV-2 RBDs. The assay went through the following steps. 1) baseline: 1 min with 1x  
538 kinetic buffer; 2) loading: 150 seconds with IgGs; 3) wash: 1 min wash of unbound IgGs  
539 with 1x kinetic buffer; 4) baseline: 1 min with 1x kinetic buffer; 5) association: 2 mins with  
540 RBDs; and 6) dissociation: 2 min with 1x kinetic buffer. The binding between IgGs and  
541 wild-type RBD acted as a reference for comparison of the binding kinetics to RBD variants.  
542

543 To obtain kinetics of binding of CV05-163 to SARS-CoV-2 RBD, briefly, His<sub>6</sub>-tagged RBD  
544 protein at 20 µg/mL in 1x kinetics buffer (1x PBS, pH 7.4, 0.01% BSA and 0.002% Tween  
545 20) was loaded onto Ni-NTA biosensors and incubated with CV05-163 Fab at  
546 concentrations of 500 nM with 2-fold gradient dilutions to 31.25 nM. The assay consisted  
547 of five steps: 1) baseline: 60 s with 1x kinetics buffer; 2) loading: 240 s with His<sub>6</sub>-tagged  
548 RBD protein; 3) baseline: 60 s with 1x kinetics buffer; 4) association: 180 s with Fab; and  
549 5) dissociation: 180 s with 1x kinetics buffer. For estimating  $K_D$ , a 1:1 binding model was  
550 used.

551

## 552 **Pseudovirus neutralization assay**

553 Pseudovirus (PSV) preparation and assay were performed as previously described with  
554 minor modifications (9). Pseudovirions were generated by co-transfection of HEK293T  
555 cells with plasmids encoding MLV-gag/pol, MLV-CMV-Luciferase, and SARS-CoV-2  
556 spike WT (GenBank: MN908947) or variants with an 18-AA truncation at the C-terminus.  
557 Supernatants containing pseudotyped virus were collected 48 h after transfection and  
558 frozen at -80°C for long-term storage. PSV neutralizing assay was carried out as follows.  
559 25 µl of mAbs serially diluted in DMEM with 10% heat-inactivated FBS, 1% Q-max, and  
560 1% P/S were incubated with 25 µl of SARS-CoV-2 PSV at 37°C for 1 h in 96-well half-  
561 well plate (Corning, 3688). After incubation, 10,000 Hela-hACE2 cells, generated by  
562 lentivirus transduction of wild-type Hela cells and enriched by fluorescence-activated cell

563 sorting (FACS) using biotinylated SARS-CoV-2 RBD conjugated with streptavidin-Alexa  
564 Fluor 647 (Thermo, S32357), were added to the mixture with 20 µg/ml Dextran (Sigma,  
565 93556-1G) to enhance infectivity. At 48 h post incubation, the supernatant was  
566 aspirated, and HeLa-hACE2 cells were then lysed in luciferase lysis buffer (25 mM  
567 Glegly pH 7.8, 15 mM MgSO<sub>4</sub>, 4 mM EGTA, 1% Triton X-100). Bright-Glo (Promega,  
568 PR-E2620) was added to the mixture following the manufacturer's instruction, and  
569 luciferase expression was read using a luminometer. Samples were tested in duplicate,  
570 and assays were repeated at least twice for confirmation. Neutralization ID<sub>50</sub> titers or IC<sub>50</sub>  
571 values were calculated using “One-Site Fit LogIC<sub>50</sub>” regression in GraphPad Prism 9.

572

### 573 **Expression and purification of recombinant S protein for negative-stain electron** 574 **microscopy**

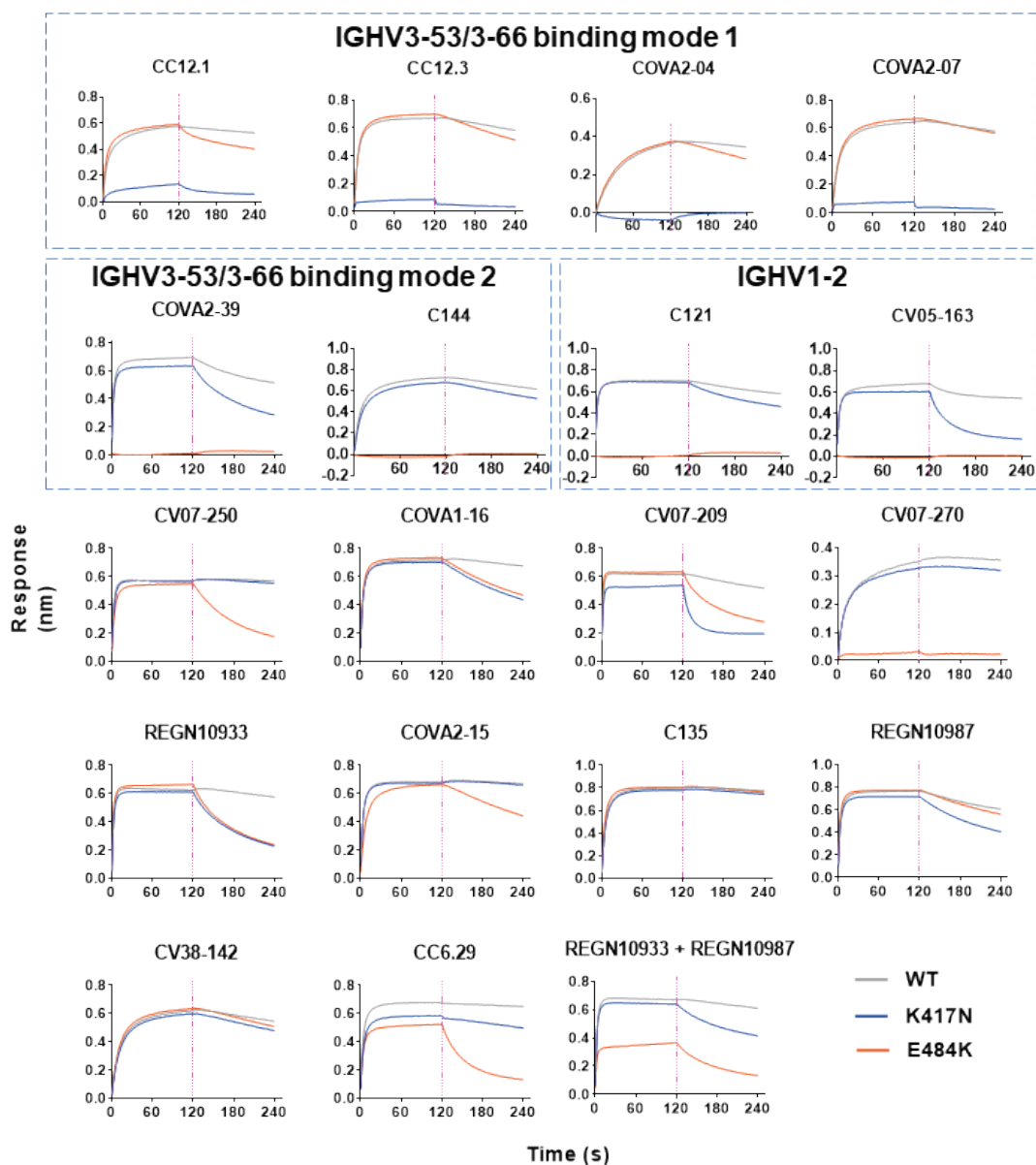
575 The S protein construct used for negative-stain EM was SARS-CoV-2-6P-Mut7. The  
576 construct contains the mammalian-codon-optimized gene encoding residues 1-1208 of  
577 the S protein (GenBank: QHD43416.1), an HRV3C cleavage site, and a Twin-strep tag  
578 subcloned into the eukaryotic expression vector pcDNA3.4. To prevent cleavage, three  
579 amino-acid mutations were introduced into the S1-S2 cleavage site (RRAR to GSAS).  
580 For S protein stability, six proline mutations (F817P, A892P, A899P, A942P, K986P,  
581 V987P) and a disulfide mutation between T883 and V705 (mutated to cysteines) were  
582 introduced (10-12). The S plasmid was transfected into HEK293F cells and the  
583 supernatant was harvested 6 days post-transfection. To purify the S protein, the  
584 supernatant was run through a Stereotactic XT 4FLOW column (IBA Lifesciences)  
585 followed by size exclusion chromatography using a Superose 6 increase 16/600 µg.  
586 column (GE Healthcare Biosciences). Protein fractions corresponding to the trimeric S  
587 protein were collected and concentrated.

588



589 **nsEM sample preparation and data collection**

590 SARS-CoV-2-6P-Mut7 S protein was complexed with a 3-fold molar excess of Fab and  
591 incubated for 30 minutes at room temperature. The complex was diluted to  
592 approximately 0.03 mg/mL with 1x TBS pH 7.4 and applied onto carbon-coated 400-  
593 mesh copper grids. The grids were stained with 2% (w/v) uranyl-formate for 60 seconds  
594 immediately following sample application. Grids were imaged at 200 keV on a FEI  
595 Tecnai T20 using a Tietz TVIPS CMOS 4k × 4k camera at 62,000× magnification, -1.50  
596 μm defocus, and a total dose of 25 e<sup>-</sup>/Å<sup>2</sup>. Micrographs were collected using Legion (13)  
597 and transferred to the Appion database (14) for processing. Particles were picked using  
598 a difference-of-Gaussians picker (DoG-picker) (15) and stacked with a box size of 256  
599 pixels, then transferred to Relion (16) for 2D and 3D classification. Select 3D classes  
600 were refined and analyzed in UCSF Chimera (17) for making figures. A published  
601 prefusion spike model (PDB: 6VYB) (18) was used in the structural analysis.



602

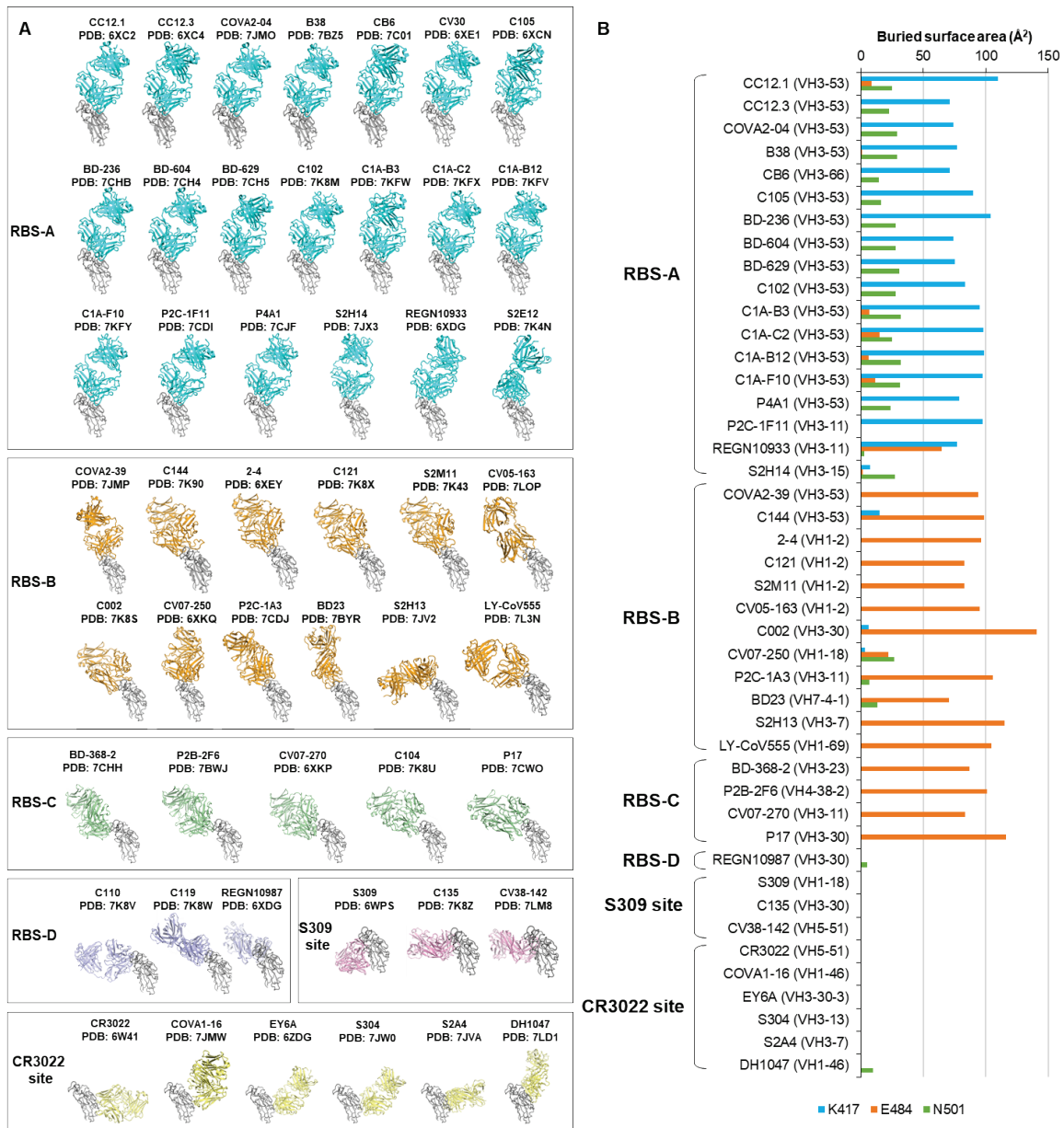
603 **Supplementary Figure 1. Sensorgrams for binding of IgGs to wild-type and**

604 **mutated SARS-CoV-2 RBD.** Binding kinetics were measured by biolayer interferometry

605 with IgGs loaded on the biosensor and RBD proteins in solution. Wild-type SARS-CoV-2

606 RBD, K417N, and E484K are shown in grey, blue, and orange, respectively.

607 Representative results of three replicates for each experiment are shown.



608

609 **Supplementary Figure 2. Epitope classification of RBD-targeting antibodies. (A)**

610 The classification is based on initial categories and assignments in (19). The SARS-

611 CoV-2 RBD (grey) is shown in the same relative orientation in each panel. Antibodies

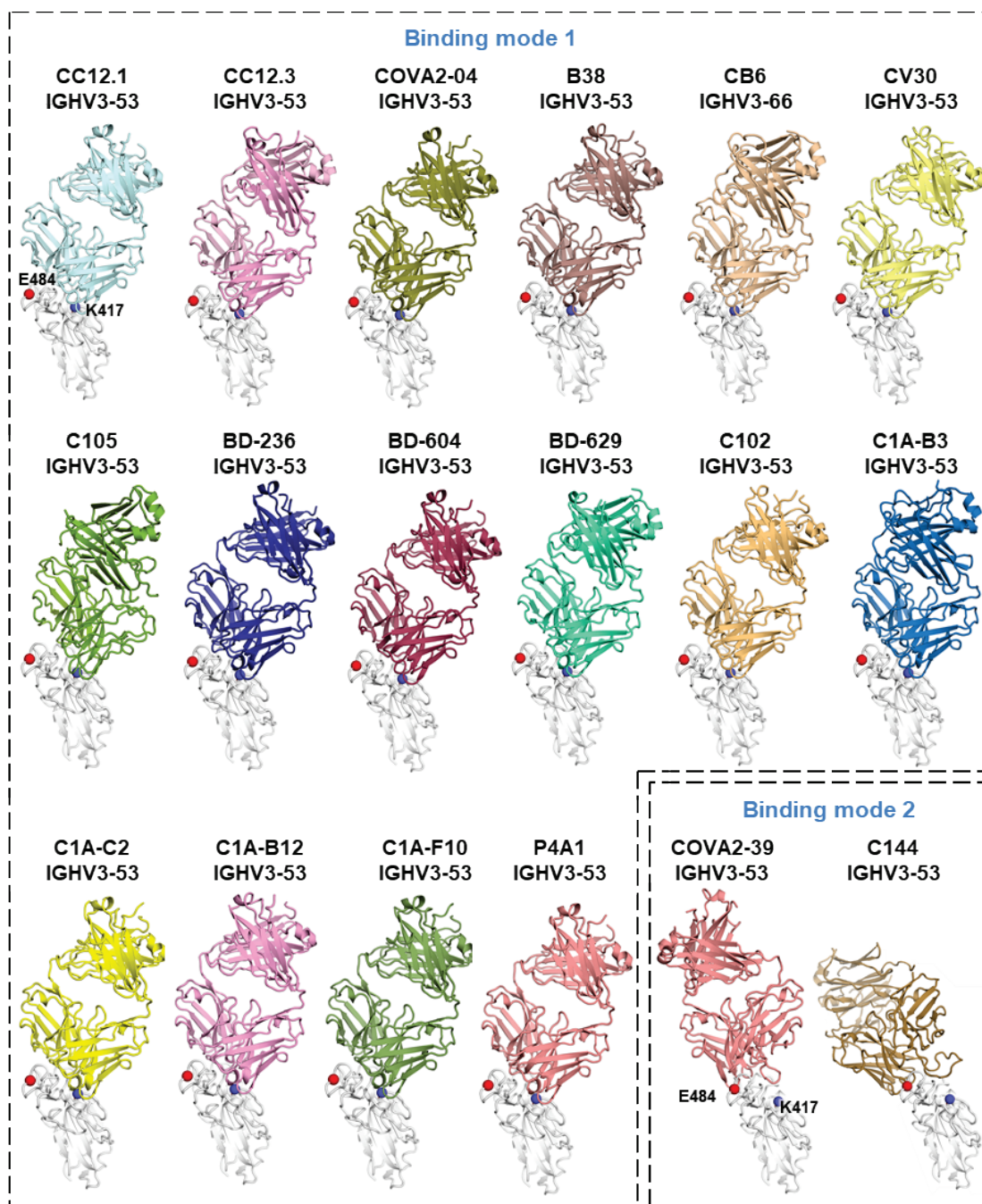
612 are color-coded by their respective epitopes. (B) Buried surface area (BSA) of K417,

613 E484, and N501 of the SARS-CoV-2 RBD by SARS-CoV-2 targeting antibodies as

614 calculated by the PISA program (8). PDB codes for the structures used for the BSA

615 calculation are shown in panel (A). Structures of S2E12 (PDB 7K4N), C104 (PDB

616 7K8U), C110 (PDB 7K8V), and C119 (PDB 7K8W) are not included in the calculation  
617 because residues or side chains of the epitope and/or paratope residues were truncated  
618 in the published structures. Heavy chain germline genes that encode each antibody are  
619 shown in brackets.

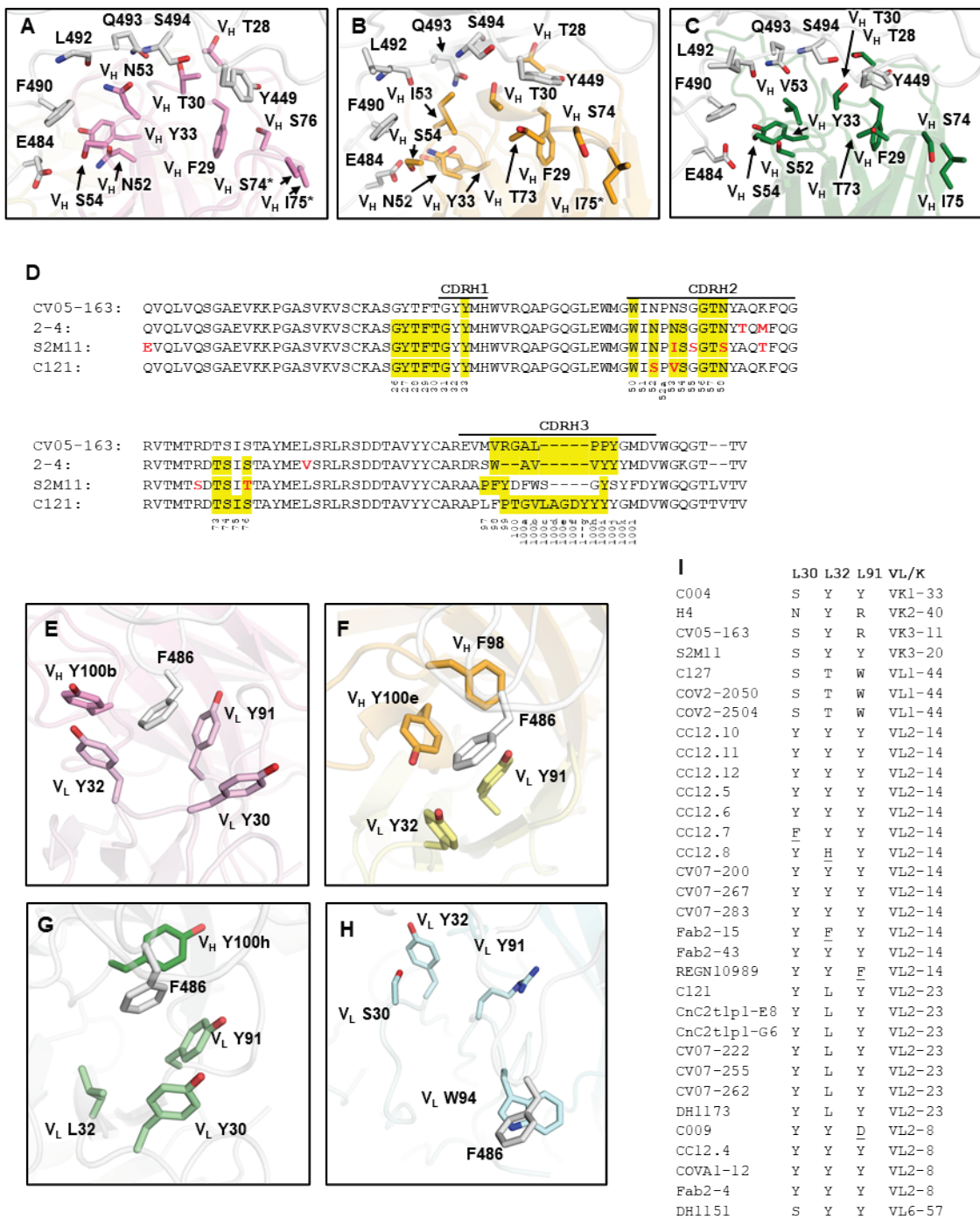


620

621 **Supplementary Figure 3. Structures of IGHV3-53/3-66 antibodies in complex with**  
622 **SARS-CoV-2 RBD.** 16 out of 18 RBD-targeting IGHV3-53/3-66 antibodies with available  
623 structures in the PDB bind to the same epitope using a nearly identical angle of  
624 approach (binding mode 1) to SARS-CoV-2 RBD (white). RBD-K417 is intimately  
625 involved in the epitope. The other two antibodies COVA2-39 and C144 bind to the

626 opposite site of the RBS (binding mode 2) and, in this binding mode, RBD-E484 is a key  
627 contributor to the epitope. RBDs are shown in the same relative orientation in each  
628 panel. E484 (left) and K417 (right) are represented by red and blue spheres,  
629 respectively, and are also labeled in the first panel. All available RBD-targeting IGHV3-  
630 53/3-66 antibody structures in the PDB at time of analysis (January 2021) are shown:  
631 CC12.1 (PDB ID: 6XC3), CC12.3 (PDB ID: 6XC4) (20), COVA2-04 (PDB ID: 7JMO)  
632 (21), B38 (PDB ID: 7BZ5) (22), CB6 (PDB ID: 7C01) (23), CV30 (PDB ID: 6XE1) (24),  
633 C105 (PDB ID: 6XCN) (25), BD-236 (PDB ID: 7CHB), BD-604 (PDB ID: 7CH4), BD-629  
634 (PDB ID: 7CH5) (26), C102 (PDB ID: 7K8M) (27), C1A-B3 (PDB ID: 7KFW), C1A-C2  
635 (PDB ID: 7KFX), C1A-B12 (PDB ID: 7KFV), C1A-F10 (PDB ID: 7KFY) (28), P4A1 (PDB  
636 ID: 7JCF) (29), COVA2-39 (PDB ID: 7JMP) (21), and C144 (PDB ID: 7K90) (25).





637

638 **Supplementary Figure S4. Molecular interactions between IGHV1-2 antibodies and**

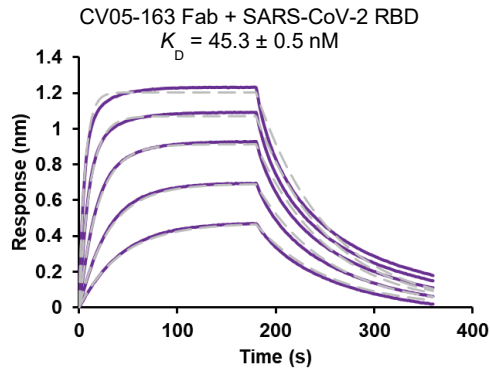
639 **SARS-CoV-2 RBD.** In panels A-C and E-H, RBD residues are shown in white. Details of

640 antibody interactions with the RBS of the SARS-CoV-2 RBD are illustrated for: **(A)** 2-4

641 **(PDB 6XEY) (30) in pink, (B) S2M11 (PDB 7K43) (31) in orange, and (C) C121 (PDB**

642 7K8X) (27) in green. **(D)** Sequence alignment of CV05-163, 2-4, and S2M11 variable  
643 heavy ( $V_H$  region). The regions that correspond to CDR H1, H2, H3, L1, L2, and L3 are  
644 indicated in Kabat numbering. Antibody residues that interact with the RBD are  
645 highlighted in yellow [residues with a BSA  $> 0 \text{ \AA}^2$  as calculated by the PISA program (8)].  
646 Somatic hypermutated residues are highlighted in red. **(E–H)** Interactions of SARS-CoV-  
647 2 RBD F486 with **(E)** 2-4, **(F)** S2M11, **(G)** C121, and **(H)** CV05-163. The four structures  
648 are superimposed on the RBD and shown in the same overall view. **(I)** Light-chain  
649 residues at positions 30, 32, and 91 (Kabat numbering) in all RBD-targeting IGHV1-2  
650 neutralizing antibodies with sequence information [summarized in CoV-AbDab (32)].  
651 Somatic hypermutated residues are underlined. Among IGHV1-2 RBD antibodies  
652 with reported neutralization activity, nine different light chains have been observed to  
653 date, although with preference for IGLV2-14, IGLV2-23, and IGLV2-8, which account for  
654 over 76% of the light chains that pair with IGHV1-2. Importantly, germline residues at  
655 positions 30, 32, and 91 of IGLV2-14, IGLV2-23, and IGLV2-8 are all aromatic or  
656 hydrophobic residues, further delineating why IGHV1-2 antibodies paired with these  
657 specific light chains are naturally favored for this canonical RBD-binding mode for  
658 neutralization of SARS-CoV-2. In contrast, CV05-163 represents a small subset of  
659 IGHV1-2 RBD-targeting antibodies without hydrophobic residues at positions 30 or 91 of  
660 the light chain that form a hydrophobic pocket for anchoring RBD-F486 in most IGHV1-2  
661 antibodies that bind in the canonical mode.





662

663 **Supplementary Figure 5. Sensorgrams for binding of CV05-163 Fab to SARS-CoV-**

664 **2 RBD.** Binding kinetics of CV05-163 Fab against SARS-CoV-2 RBD were measured by

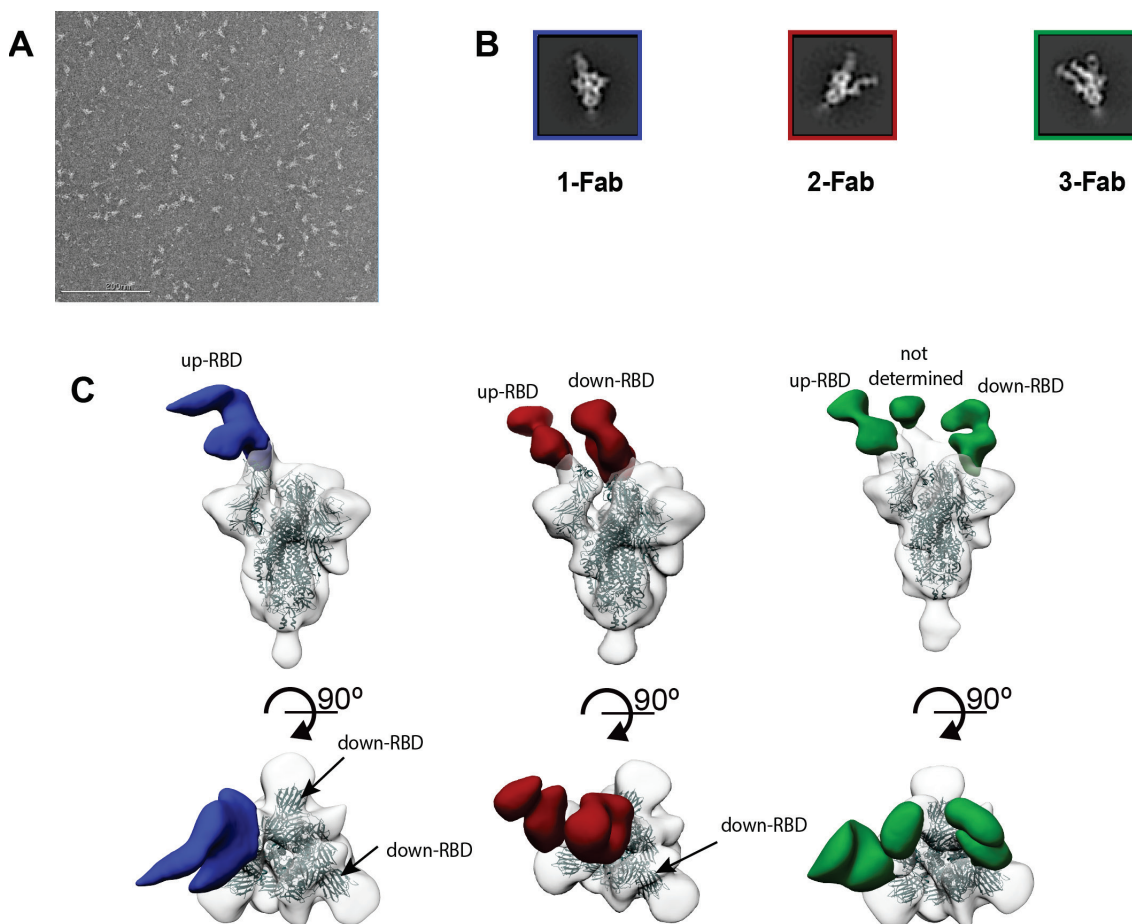
665 biolayer interferometry (BLI). Y-axis represents the response. Purple solid lines

666 represent the response curves and grey dashed lines represent the 1:1 binding model.

667 Binding kinetics were measured for five concentrations of Fab at 2-fold dilution ranging

668 from 500 nM to 31.25 nM. The  $K_D$  of the fitting is indicated. Representative results of

669 three replicates for each experiment are shown.



670

671 **Supplementary Figure 6. nsEM analysis of CV05-163 in complex with SARS-CoV-2**

672 **S trimer. (A)** Representative negative stain-EM micrograph. **(B)** Select 2D class averages

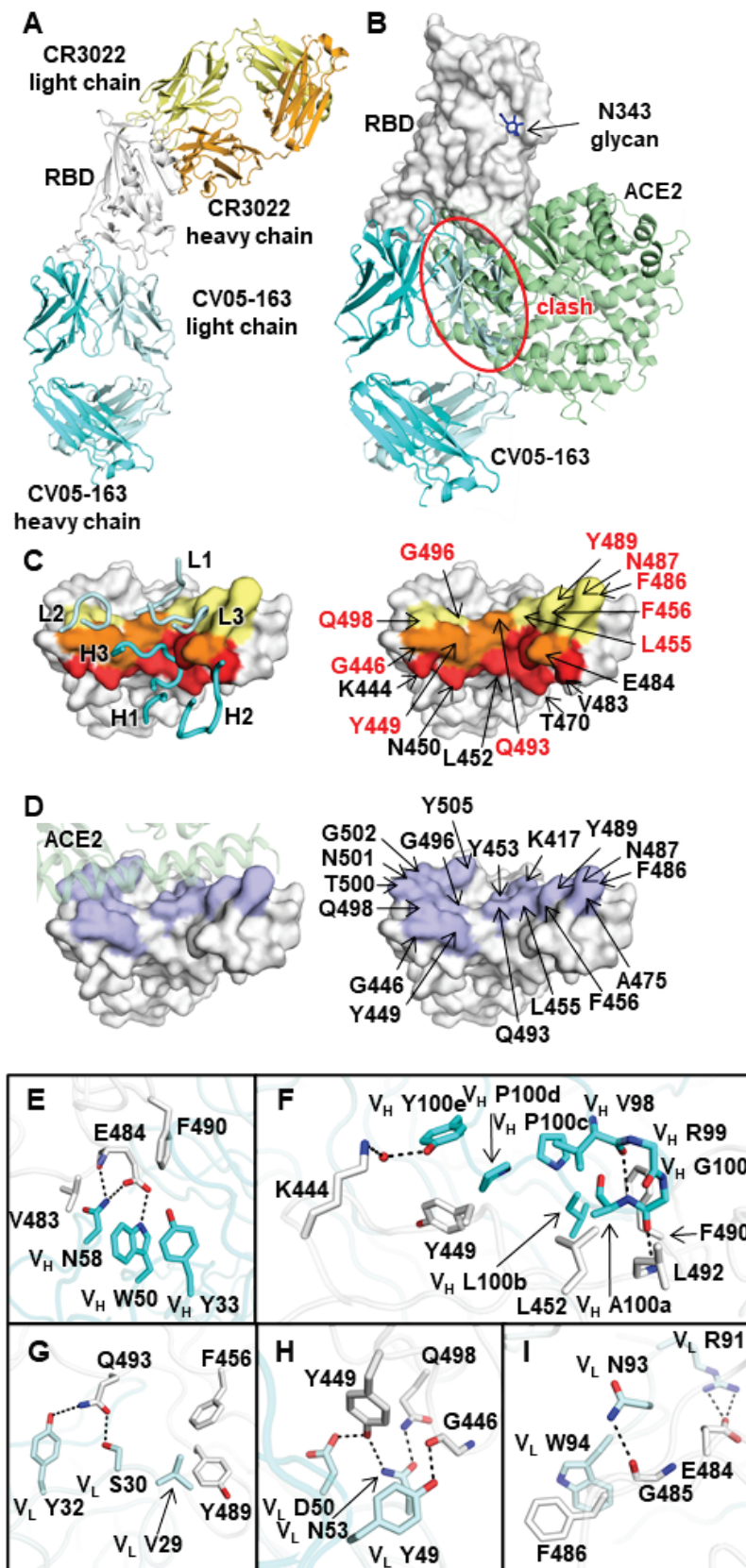
673 of single-particle nsEM analysis of CV05-163 complexed with S trimer. 2D classes

674 corresponding to the 1-, 2-, and 3-Fab binding stoichiometries are highlighted in a blue,

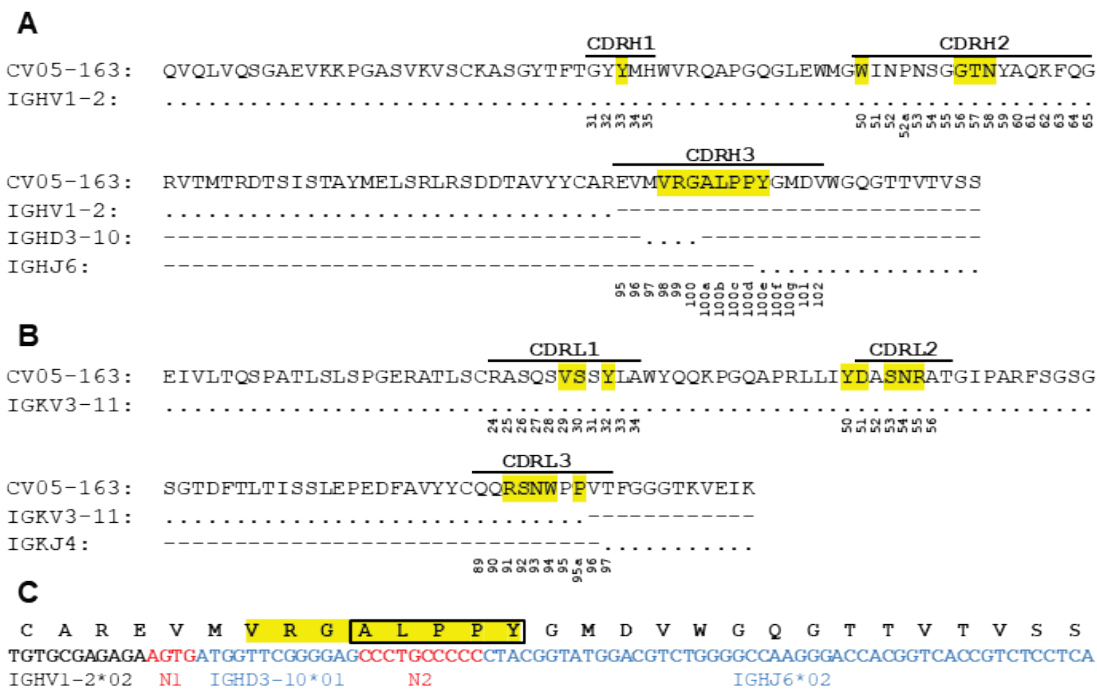
675 red, and green box, respectively. **(C)** 3D nsEM reconstructions of 1, 2, and 3 Fab CV05-

676 163 bound to the SARS-CoV-2 S trimer. CV05-163 binds both up- and down-RBD in

677 various stoichiometries, including molar ratios of 1:1, 2:1, and 3:1 (Fab : S trimer).

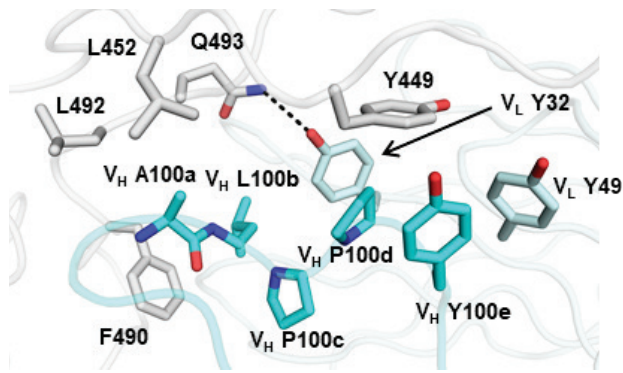


679 **Supplementary Figure 7. Crystal structure of SARS-CoV-2 RBD in complex with**  
680 **Fabs CV05-163 and CR3022. (A)** The binding site of CV05-163 (Fab heavy and light  
681 chains shown in cyan and pale cyan, respectively) on the RBD (white) is distinct from that  
682 of CR3022 (Fab heavy and light chains shown in orange and yellow, respectively). **(B)** The  
683 ACE2/RBD complex structure (PDB 6M0J) (33) is superimposed on the CV05-163/RBD  
684 complex. CV05-163 (cyan) would clash with ACE2 (green) if bound simultaneously with  
685 the RBD (indicated by red ellipse). The N-glycan at N343 of the RBD is in dark blue. **(C)**  
686 Epitope of CV05-163. Epitope residues contacting the heavy chain are in red and the light  
687 chain in yellow, while residues contacting both heavy and light chains are in orange. On  
688 the left panel, CDR loops are labeled. On the right panels, epitope residues are labeled.  
689 For clarity, only representative epitope residues are labeled. Epitope residues that are  
690 also involved in ACE2 binding are labeled in red. **(D)** ACE2-binding residues on the RBD  
691 are in lilac. On the left panel, ACE2 is represented by an olive semi-transparent surface.  
692 On the right panel, ACE2-binding residues are labeled. The 17 ACE2-binding residues are  
693 as described previously (PDB 6M0J) (33). **(E and F)** Interactions between the RBD and  
694 heavy chain of CV05-163 for **(E)** CDR H1 and H2 and **(F)** CDR H3. **(G to I)** Interactions  
695 between RBD and light chain of CV05-163 for **(G)** CDR L1, **(H)** CDR L2 and **(I)** CDR L3.



696

697 **Supplementary Figure 8. Sequence analysis of a germline antibody CV05-163**  
 698 **targeting the SARS-CoV-2 RBD. (A and B)** CV05-163 V<sub>H</sub> and V<sub>L</sub> sequence alignment  
 699 with corresponding putative germline gene segments. The sequences of both V<sub>H</sub> and V<sub>L</sub>  
 700 chains of CV05-163 have no somatic hypermutations compared to their germline genes.  
 701 The regions that correspond to CDR H1, H2, H3, L1, L2, and L3 are indicated. Residues  
 702 that interact with the RBD are highlighted in yellow. Residue positions in the CDRs are  
 703 labeled according to the Kabat numbering scheme. Conserved residues are represented  
 704 by dots (.) and non-germline encoded residues are indicated by dashes (-). **(C)** Sequence  
 705 of the V-D-J junction of CV05-163, with putative gene segments (blue) and N-regions (red)  
 706 indicated. Residues that interact with the RBD are highlighted in yellow. The shared  
 707 junctional motif in CDR H3 (“ALPPY”) arises mainly from N-additions and is highlighted in  
 708 a black box.

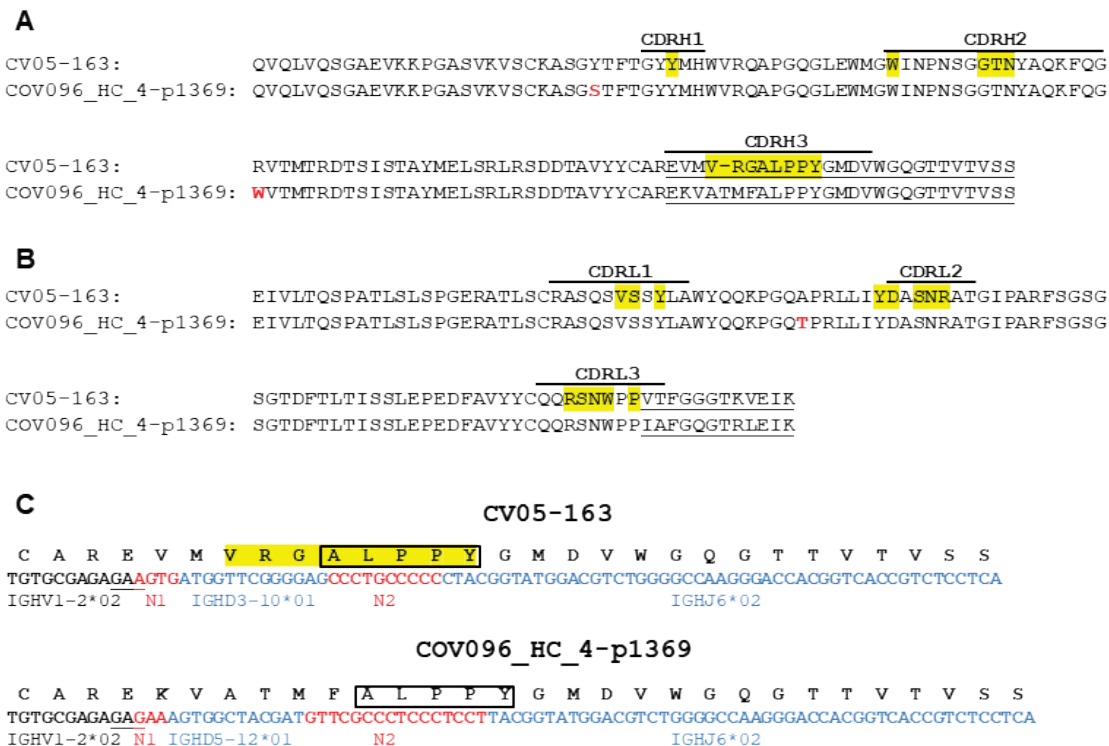


710 **Supplementary Figure 9. Interactions between the ALPPY motif and SARS-CoV-2**

711 **RBD.** The RBD is in white and antibody residues in cyan (heavy chain) and pale cyan

712 (light chain), respectively. A hydrogen bond is represented by a dashed line.



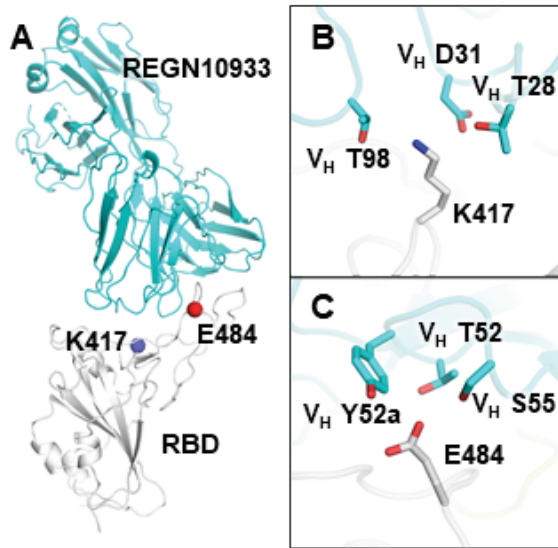


713

714 **Supplementary Figure 10. Convergence of the N-addition encoded ALPPY motif in**  
715 **RBD-targeting IGHV1-2 antibodies.** Conservation of a non-germline encoded motif is  
716 expected to be extremely rare, but an “ALPPY” motif encoded mainly by N-additions is  
717 found in CDR H3 of two RBD antibodies CV05-163 and COV096\_HC\_4-p1369 (34) from  
718 different individuals. CV05-163 and COV096\_HC\_4-p1369 are both encoded by IGHV1-  
719 2/IGKV3-11. **(A and B)** V<sub>H</sub> and V<sub>L</sub> sequence alignment of CV05-163 with  
720 COV096\_HC\_4-p1369. Somatic hypermutated residues are highlighted in red. Regions  
721 that correspond to CDR H1, H2, H3, L1, L2, and L3 are indicated. Residues of CV05-  
722 163 that interact with the RBD in the CV05-163/RBD complex structure are highlighted in  
723 yellow [defined here as residues with a BSA > 0 Å<sup>2</sup> as calculated by the PISA program  
724 (8)]. Residue positions in the CDRs are labeled according to the Kabat numbering  
725 scheme. Non-V-gene encoded residues are underlined. **(C)** Sequences of the V-D-J  
726 junction of CV05-163 and COV096\_HC\_4-p1369, with putative D and J gene segments  
727 (blue) and N-regions (red) indicated. CV05-163 residues that interact with the RBD are

728 highlighted in yellow. The shared junctional motif (“ALPPY”) is boxed. Germline residue  
729 V<sub>L</sub> R91 of CV05-163 that interacts with RBD-E484 is also stabilized by V<sub>H</sub> E95, which is  
730 also partially encoded by N-additions and conserved between CV05-163 and  
731 COV096\_HC\_4-p1369. Nucleotides that encode V<sub>H</sub> E95 of CV05-163 and  
732 COV096\_HC\_4-p1369 are underlined.





733

734 **Supplementary Figure 11. K417 and E484 are both involved in recognition by**

735 **antibody REGN10933. (A)** An overall view of the interaction between REGN10933

736 (cyan) and SARS-CoV-2 RBD (white) (PDB 6XDG) (35). Residues K417 and E484 are

737 represented by blue and red spheres, respectively. **(B-C)** Interactions of **(B)** RBD-K417

738 and **(C)** RBD-E484 with REGN10933. Hydrogen bonds are not shown due to the limited

739 resolution (3.9 Å). Kabat numbering is assigned to the residues of REGN10933.

740 **Supplementary Table 1. X-ray data collection and refinement statistics**

<b>Data collection</b>	CV05-163 + RBD + CR3022
Beamline	APS23ID-B
Wavelength (Å)	1.0337
Space group	P 1 2 <sub>1</sub> 1
Unit cell parameters	
a, b, c (Å)	86.0, 132.9, 111.3
α, β, γ (°)	90, 100.7, 90
Resolution (Å) <sup>a</sup>	50.0-2.25 (2.29-2.25)
Unique reflections <sup>a</sup>	115,419 (10,628)
Redundancy <sup>a</sup>	3.2 (2.4)
Completeness (%) <sup>a</sup>	98.9 (91.5)
<I/σ <sub>I</sub> > <sup>a</sup>	7.1 (1.0)
R <sub>sym</sub> <sup>b</sup> (%) <sup>a</sup>	14.6 (63.8)
R <sub>pim</sub> <sup>b</sup> (%) <sup>a</sup>	9.4 (46.6)
CC <sub>1/2</sub> <sup>c</sup> (%) <sup>a</sup>	97.8 (61.5)
<b>Refinement statistics</b>	
Resolution (Å)	49.4-2.25
Reflections (work)	115,390
Reflections (test)	10,625
R <sub>cryst</sub> <sup>d</sup> / R <sub>free</sub> <sup>e</sup> (%)	22.1/26.5
No. of atoms	17,694
RBD	3,101
Fab	13,328
Glycan	28
Solvent	1,237
Average B-values (Å <sup>2</sup> )	34
RBD	31
CV05-163 Fab	33
CR3022 Fab	35
Glycan	47
Solvent	35
Wilson B-value (Å <sup>2</sup> )	29
<b>RMSD from ideal geometry</b>	
Bond length (Å)	0.004
Bond angle (°)	0.82
<b>Ramachandran statistics (%)</b>	
Favored	97.1
Outliers	0.09
<b>PDB code</b>	7LOP

741

<sup>a</sup> Numbers in parentheses refer to the highest resolution shell.

742

<sup>b</sup>  $R_{sym} = \frac{\sum_{hkl} \sum_i |I_{hkl,i} - \langle I_{hkl} \rangle|}{\sum_{hkl} \sum_i I_{hkl,i}}$  and  $R_{pim} = \frac{\sum_{hkl} (1/(n-1))^{1/2} \sum_i |I_{hkl,i} - \langle I_{hkl} \rangle|}{\sum_{hkl} \sum_i I_{hkl,i}}$ , where  $I_{hkl,i}$  is the scaled intensity of the  $i^{\text{th}}$  measurement of reflection  $h, k, l$ ,  $\langle I_{hkl} \rangle$  is the average intensity for that reflection, and  $n$  is the redundancy.

743

744

<sup>c</sup> CC<sub>1/2</sub> = Pearson correlation coefficient between two random half datasets.

745

746

<sup>d</sup>  $R_{cryst} = \frac{\sum_{hkl} |F_o - F_c|}{\sum_{hkl} |F_o|} \times 100$ , where  $F_o$  and  $F_c$  are the observed and calculated structure factors, respectively.

747

<sup>e</sup>  $R_{free}$  was calculated as for  $R_{cryst}$ , but on a test set comprising 5% of the data excluded from refinement.

748  
749  
750

**Supplementary Table 2. Hydrogen bonds and salt bridges identified at the antibody-RBD interface using the PISA program.**

SARS-CoV-2 RBD	Distance [Å]	CV05-163
<b>Hydrogen bonds</b>		
GLU484[OE2]	3.0	VH TRP50[NE1]
GLU484[O]	3.0	VH ASN58[ND2]
LEU492[N]	2.7	VH GLY100[O]
GLY446[O]	2.7	VK: TYR49[OH]
TYR449[OH]	3.4	VK: ASN53[ND2]
GLU484[OE2]	3.0	VK: ARG91[NH1]
GLU484[OE2]	3.1	VK: ARG91[NH2]
GLY485[O]	3.3	VK: ASN93[ND2]
GLN493[OE1]	2.9	VK: SER30[OG]
GLN493[NE2]	3.7	VK: TYR32[OH]
TYR449[OH]	2.5	VK: ASP50[OD2]
GLN498[NE2]	2.7	VK: ASN53[OD1]
<b>Salt bridges</b>		
GLU484[OE2]	3.0	VK: ARG91[NH1]
GLU484[OE2]	3.1	VK: ARG91[NH2]

751

## 752 SUPPLEMENTARY REFERENCES

- 753 1. M. Yuan *et al.*, A highly conserved cryptic epitope in the receptor binding  
754 domains of SARS-CoV-2 and SARS-CoV. *Science* **368**, 630-633 (2020).
- 755 2. D. C. Ekiert *et al.*, A highly conserved neutralizing epitope on group 2 influenza A  
756 viruses. *Science* **333**, 843-850 (2011).
- 757 3. Z. Otwinowski, W. Minor, Processing of X-ray diffraction data collected in  
758 oscillation mode. *Methods Enzymol* **276**, 307-326 (1997).
- 759 4. A. J. McCoy *et al.*, Phaser crystallographic software. *J Appl Crystallogr* **40**, 658-  
760 674 (2007).
- 761 5. D. Schrott *et al.*, Repertoire Builder: high-throughput structural modeling of B and  
762 T cell receptors. *Mol Sys Des Eng* **4**, 761-768 (2019).
- 763 6. P. Emsley, B. Lohkamp, W. G. Scott, K. Cowtan, Features and development of  
764 Coot. *Acta Crystallogr D Biol Crystallogr* **66**, 486-501 (2010).
- 765 7. P. D. Adams *et al.*, PHENIX: a comprehensive Python-based system for  
766 macromolecular structure solution. *Acta Crystallogr D Biol Crystallogr* **66**, 213-  
767 221 (2010).
- 768 8. E. Krissinel, K. Henrick, Inference of macromolecular assemblies from crystalline  
769 state. *J Mol Biol* **372**, 774-797 (2007).
- 770 9. T. F. Rogers *et al.*, Isolation of potent SARS-CoV-2 neutralizing antibodies and  
771 protection from disease in a small animal model. *Science* **369**, 956-963 (2020).
- 772 10. J. Pallesen *et al.*, Immunogenicity and structures of a rationally designed  
773 prefusion MERS-CoV spike antigen. *Proc Natl Acad Sci U S A* **114**, E7348-  
774 E7357 (2017).
- 775 11. C.-L. Hsieh *et al.*, Structure-based design of prefusion-stabilized SARS-CoV-2  
776 spikes. *Science* **369**, 1501-1505 (2020).
- 777 12. S. Bangaru *et al.*, Structural analysis of full-length SARS-CoV-2 spike protein  
778 from an advanced vaccine candidate. *Science* **370**, 1089-1094 (2020).
- 779 13. C. Suloway *et al.*, Automated molecular microscopy: the new Legion system. *J*  
780 *Struct Biol* **151**, 41-60 (2005).
- 781 14. G. C. Lander *et al.*, Appion: an integrated, database-driven pipeline to facilitate  
782 EM image processing. *J Struct Biol* **166**, 95-102 (2009).
- 783 15. N. R. Voss, C. K. Yoshioka, M. Radermacher, C. S. Potter, B. Carragher, DoG  
784 Picker and TiltPicker: software tools to facilitate particle selection in single  
785 particle electron microscopy. *J Struct Biol* **166**, 205-213 (2009).
- 786 16. J. Zivanov *et al.*, New tools for automated high-resolution cryo-EM structure  
787 determination in RELION-3. *eLife* **7**, e42166 (2018).

- 788 17. E. F. Pettersen *et al.*, UCSF Chimera--a visualization system for exploratory  
789 research and analysis. *J Comput Chem* **25**, 1605-1612 (2004).
- 790 18. A. C. Walls *et al.*, Structure, function, and antigenicity of the SARS-CoV-2 spike  
791 glycoprotein. *Cell* **181**, 281-292 e286 (2020).
- 792 19. M. Yuan, H. Liu, N. C. Wu, I. A. Wilson, Recognition of the SARS-CoV-2 receptor  
793 binding domain by neutralizing antibodies. *Biochem Biophys Res Commun*  
794 10.1016/j.bbrc.2020.10.012, (2020).
- 795 20. M. Yuan *et al.*, Structural basis of a shared antibody response to SARS-CoV-2.  
796 *Science* **369**, 1119-1123 (2020).
- 797 21. N. C. Wu *et al.*, An alternative binding mode of IGHV3-53 antibodies to the  
798 SARS-CoV-2 receptor binding domain. *Cell Rep* **33**, 108274 (2020).
- 799 22. Y. Wu *et al.*, A noncompeting pair of human neutralizing antibodies block COVID-  
800 19 virus binding to its receptor ACE2. *Science* **368**, 1274-1278 (2020).
- 801 23. R. Shi *et al.*, A human neutralizing antibody targets the receptor-binding site of  
802 SARS-CoV-2. *Nature* **584**, 120-124 (2020).
- 803 24. N. K. Hurlburt *et al.*, Structural basis for potent neutralization of SARS-CoV-2 and  
804 role of antibody affinity maturation. *Nat Commun* **11**, 5413 (2020).
- 805 25. C. O. Barnes *et al.*, Structures of human antibodies bound to SARS-CoV-2 spike  
806 reveal common epitopes and recurrent features of antibodies. *Cell* **182**, 828-842  
807 e816 (2020).
- 808 26. S. Du *et al.*, Structurally resolved SARS-CoV-2 antibody shows high efficacy in  
809 severely infected hamsters and provides a potent cocktail pairing strategy. *Cell*  
810 **183**, 1013–1023.e1013 (2020).
- 811 27. C. O. Barnes *et al.*, SARS-CoV-2 neutralizing antibody structures inform  
812 therapeutic strategies. *Nature* **588**, 682–687 (2020).
- 813 28. S. A. Clark *et al.*, Molecular basis for a germline-biased neutralizing antibody  
814 response to SARS-CoV-2. *bioRxiv* 10.1101/2020.11.13.381533, (2020).
- 815 29. Y. Guo *et al.*, A SARS-CoV-2 neutralizing antibody with exceptional spike binding  
816 coverage and optimized therapeutic potentials. *Research Square*  
817 10.21203/rs.3.rs-78945/v1, (2020).
- 818 30. L. Liu *et al.*, Potent neutralizing antibodies against multiple epitopes on SARS-  
819 CoV-2 spike. *Nature* **584**, 450-456 (2020).
- 820 31. M. A. Tortorici *et al.*, Ultrapotent human antibodies protect against SARS-CoV-2  
821 challenge via multiple mechanisms. *Science* **370**, 950-957 (2020).

- 822 32. M. I. J. Raybould, A. Kovaltsuk, C. Marks, C. M. Deane, CoV-AbDab: the  
823 coronavirus antibody database. *Bioinformatics* 10.1093/bioinformatics/btaa739,  
824 (2020).
- 825 33. J. Lan *et al.*, Structure of the SARS-CoV-2 spike receptor-binding domain bound  
826 to the ACE2 receptor. *Nature* **581**, 215-220 (2020).
- 827 34. D. F. Robbiani *et al.*, Convergent antibody responses to SARS-CoV-2 in  
828 convalescent individuals. *Nature* **584**, 437-442 (2020).
- 829 35. J. Hansen *et al.*, Studies in humanized mice and convalescent humans yield a  
830 SARS-CoV-2 antibody cocktail. *Science* **369**, 1010-1014 (2020).